Acta Cryst. (1996). A52, 850–878

Geometrical Aspects of the Diffraction Space of Serpentine Rolled Microstructures: their Study by means of Electron Diffraction and Microscopy

S. AMELINCKX,[a]* B. DEVOUARD[a,b]† AND A. BARONNET[b]

[a]*EMAT-Laboratory, Department of Physics, University of Antwerp (RUCA), Groenenborgerlaan 171, B-2020 Antwerpen, Belgium, and* [b]*CRMC2-CNRS, Campus de Luminy, Case 913, F-91228 Marseille, France (associated with University of Aix-Marseille III)*

(Received 15 February 1996; accepted 4 June 1996)

Abstract

The geometry of the reciprocal space of cylindrically and conically rolled microstructures is described. The simpler cylindrical case is first discussed, followed by the conical case; in both cases, the observations and then the theory are described. The theory is compared with observations on chrysotiles, the structural and microstructural features of which are briefly recalled. The reciprocal space of an infinite 3D crystal consists of a lattice of discrete nodes. If a crystalline sheet is curled up into a cylindrical scroll (or into concentric cylinders), the corresponding reciprocal space is obtained by rotating this set of lattice points about a line parallel to the cylinder axis through the origin of reciprocal space. The lattice nodes thereby describe geometrical loci that, in this simple case, are circles in planes perpendicular to the rotation axis. For a general orientation of the rotation axis, each node produces its own circle. This is the case when the fibre has chiral character. For certain symmetrical orientations of the axis, 'degeneracy' occurs and two (or more) nodes may lead to the same circular locus. This is the case for achiral fibres. The curvature often causes disorder in the stacking of successive cylindrical sheets – this leads to 'coronae' instead of sharp circles – especially in the concentric cylinder case. In the diffraction pattern, these produce spots that are streaked in the sense away from the axis. In ideal cylindrical scrolls, the structures in successive layers, as viewed along a radial line **c**, are shifted relative to each other over 2π times the layer thickness; this may lead to superperiods along the normal **c** to the sheet planes if this shift is commensurate with the lattice vectors in the sheet plane, *i.e.* with its translation symmetry. The superperiod is clearly related to the sheet thickness, which may be more than one bilayer. If the 2D crystalline sheet is curled up into a cone, the reciprocal-space loci become curves that are situated on spheres of constant spatial frequency, called spherical spirals instead of the circles in the cylindrical case. Each reciprocal-lattice node describes such a spiral traced out by a node point subject to the coupled rotations about the cone axis and about the local normal to the cone surface. The equations of such spirals are derived and their symmetry properties are studied analytically. The spiral's shape is a function of the semi-apex angle of the cone. For an arbitrary cone angle, these curves are not closed; they completely fill a band on the surface of the sphere. For certain discrete cone angles, which turn out to be essentially determined by the condition of good epitaxic fit between successive sheets of the cone, the spherical spirals become closed curves. The conditions under which several node points, belonging to the same spatial frequency, trace out the same spherical spiral are discussed: *i.e.* the conditions for degeneracy are formulated. The point symmetries of the sets of spherical spirals belonging to the same spatial frequency are found to depend on characteristic values of the semi-apex angle. All turns of a conical scroll are in fact formed from a single sheet. The structure in any given turn is rotated relative to that in the adjacent turn over a constant angle, only determined by the semi-apex angle. If this rotation angle is commensurate with 2π, superperiods can be formed, visible as reinforcements in streaks that are parallel to the generators of the cone formed by the set of normals to the conical surface. Also, this superperiod depends on the thickness of the sheet as well as on its rotation symmetry. Diffuse scattering is found to be concentrated on a *V*-shaped hyperboloid-like surface, the point of the *V* being situated on a spherical spiral. The intersection of this surface with the Ewald plane leads to *V*-shaped streaks attached by their apexes to the spots. They are the homologues of the simple streaks in the cylindrical case. Under certain conditions of beam incidence, the intersection is a hyperbole branch. Spot positions have been computed for a few characteristic diffraction conditions; they are found to represent adequately the observed spot patterns. A Mercator-like projection method is

† Present address: Department of Geology, Arizona State University, Box 871404, Tempe, Arizona 85287-1404, USA.

proposed to represent the spherical spirals in a plane and to construct geometrically the intersections with the Ewald plane for different angles of incidence. Throughout the paper, the analogies and the differences between the diffraction features of cylindrical and conical scrolls are emphasized and illustrated by observations on chrysotile.

1. Introduction

The study of the properties of tubular microstructures such as those of carbon and molybdenum disulfide nanotubes and their derivatives are of great current interest for chemists, physicists and materials scientists (*e.g.* Margulis, Dluzewski, Feldman & Tenne, 1996; Iijima, 1991; Iijima & Ichihashi, 1992; Iijima & Ajayan, 1992; Zhang, Zhang, Amelinckx, Van Tendeloo & Van Landuyt, 1994; Amelinckx *et al.*, 1994; Amelinckx, Benaerts, Zhang, Van Tendeloo & Van Landuyt, 1995; Liu & Cowley, 1994*a*,*b*; Baker, 1989; Tibbets, 1984). Apart from their theoretical interest, these unusual nanostructures have potential technological applications (Ebbesen, 1994; Rodriguez, 1993). High-resolution electron microscopy (HRTEM) and selected-area electron diffraction (SAED) proved to be the most useful techniques to unravel the microstructures of these materials (Cullen, Boothroyd & Humphreys, 1994; Williams & Hyde, 1988).

It is less well known among physicists that some minerals have been known since the early 1950's to display very similar structures. Serpentine minerals, among them chrysotiles, are the best documented of these naturally occurring materials [for a comprehensive review on serpentines, see Bailey (1969, 1988*a*,*b*,*c*)]. The cylindrical structure of chrysotiles has been studied in depth by means of X-ray diffraction in a series of papers by Whittaker (1952, 1953, 1954, 1955*a*,*b*,*c*, 1956, 1957) and by Jagodzinski & Kunze (1954*a*,*b*) and, more recently, using HRTEM and SAED by Yada (Yada, 1967, 1971, 1979; Yada & Iishi, 1977).

Chrysotiles (*lato sensu*) offer a wide variety of microstructures ranging from perfectly cylindrical to helical (chiral) and conical wrappings, and they are therefore interesting test objects for exploring the diffraction effects produced by wound tubules and comparing these with high-resolution images. We have already reported on the various wrapping modes of chrysotiles (Devouard, 1996) and proposed a qualitative model for the nucleation and growth of such fibres.

In this paper, we develop an interpretation scheme for the geometry of the diffraction patterns of such microstructures and illustrate this by means of observations on various chrysotile specimens. In particular, we report in detail on conically wound synthetic chrysotile fibres.

2. Structural considerations

2.1. *Crystal structures (Whittaker, 1956; Mellini, 1982; Mellini & Zanazzi, 1987)*

The structure of the serpentine minerals lizardite, chrysotiles and antigorite with ideal composition $Mg_3(Si_2O_5)(OH)_4$ are closely related, the essential difference being the wrapping mode rather than the crystal structure (Fig. 1).

The three structures and their microstructural variants can be described in terms of strongly intralayer-bonded bilayers (1:1 layers) kept together by weaker interlayer hydrogen bonds. The idealized polar tetrahedral layer formed by hexagonal rings of corner-sharing SiO_4 tetrahedra has hexagonal symmetry. The close-packed 'brucite' $[Mg(OH)_2]$ layer has only threefold symmetry. The bilayer resulting from the juxtaposition of the two types of layer therefore has only

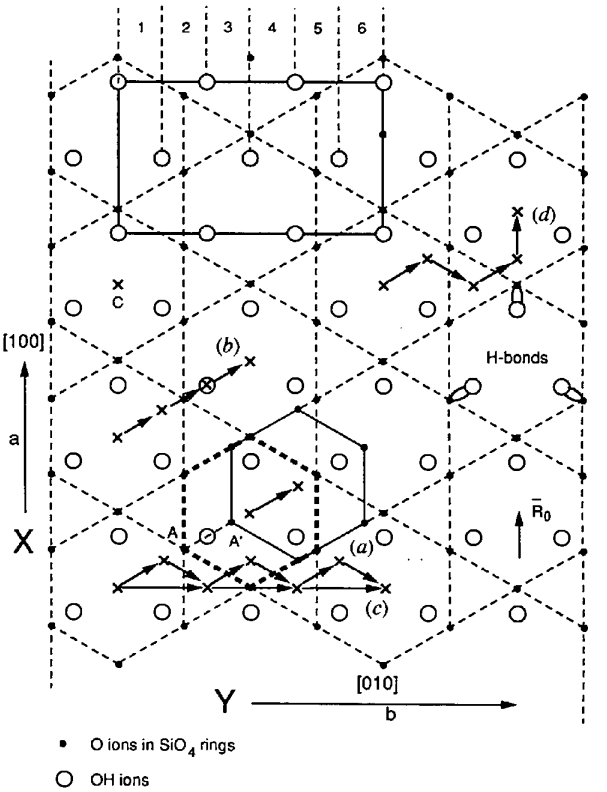

Fig. 1. The two layers of the lizardite structure, indicated by arrows in the layer sequence

...|OH–Mg–(OH, O)–Si–O|OH–Mg–(OH, O)–Si–O|...

↑ ↑

are shown as projected on the (001) plane. The unit mesh is outlined and the succession of six (010) layers along the [010] direction emphasized. In the normal stacking, the centre of the ring of SiO_4 tetrahedra project in the centre of a triangle of OH ions. Different possible dissociation schemes are indicated. An energy barrier occurs during the motion from *A* to *A'* of an O ion.

threefold symmetry. The intralayer bonding is such that the apical oxygens of the SiO_4 sheet are common to one of the O—(O—H) layers of the 'brucite' lamella. It is customary to describe this bilayer with respect to a centred rectangular unit mesh with $a = 0.52$ and $b \simeq 0.92$ nm with $b/a = 3^{1/2}$ as a result of the pseudo-hexagonal symmetry. Alternatively, a hexagonal mesh with $a \simeq 0.52$ nm could be chosen. We will often make the latter choice since this induces very little error in the lattice parameters but allows one to apply the theory also to other hexagonal layer structures since the phenomena to be discussed mainly depend on the lattice rather than on details of the structure.

The lizardite structure (Mellini, 1982; Zussman, Brindley & Comer, 1957), which we will consider as a 'reference' structure, results from the vertical stacking of such bilayers, with a thickness $t = c = 0.7$ nm, all with the same polarity, *i.e.* with all SiO_4 tetrahedra having vertices pointing in the same direction. However, many stacking variants are known (Bailey, 1969, 1988*a*,*b*,*c*; Mellini & Zanazzi, 1987); they may belong to orthorhombic, monoclinic, rhombohedral or hexagonal space groups. The bonding between successive bilayers is realized by hydrogen bonds. The building bilayer or 1:1 layer can be described with reference to a *C*-centred orthorhombic unit cell with lattice parameters $a = 0.52$, $b = 0.92$, $c = 0.7$ nm, the c parameter being equal to the bilayer thickness.

It is generally accepted that the curling up is a consequence of the misfit (3–5%) between the free tetrahedral Si_2O_5 layers ($a = 0.516$ nm) and the octahedral brucite layers ($a = 0.539$ nm), the latter having a larger unit mesh. The summits of the SiO_4 tetrahedra point towards the closest 'brucite' layer, the latter forming the convex curvature side of the bilayer.

Although the lattice parameters of the two layers are different along *all* directions in the layer plane, the curved structure will adopt a single axis of curvature, which is usually controlled by the structure of the layer. The most common variety of chrysotile is wound around the X axis (Fig. 1) and we will refer to this variety as normal chrysotile. Another variety, called parachrysotile, is wound around the Y axis (Fig. 1). Several polytypic modifications of normal chrysotile are known, including ones with an orthorhombic local cell, formally called orthochrysotile, and ones with a monoclinic local cell, formally called clinochrysotile. These polytypes differ by shifts of the successive bilayers along **X**, as well as by their orientation. Polytypic modifications of parachrysotile can occur but are not well documents [see Bailey (1969, 1988*a*,*b*,*c*) for a review of cylindrical polytypes]. We will use the terms ortho- and clinochrysotile because they do not assume a given stacking sequence (only its symmetry), which is very convenient for electron diffraction, which cannot easily distinguish the actual polytypes. In addition to the X and Y axes, the scroll or cylinder axis can also adopt a more general direction. Helically wound (chiral) cylindrical tubes now result (Fig. 2*c*).

2.2. *Wrapping models*

Since the circumferences of two successive cylinders in a tubule consisting of concentric circular cylinders differ by $2\pi t$ (t = lamella thickness, $t = nc$, n = integer), it is clear that the relative positions of two successive bilayers must change either continuously or in discrete steps. The same applies to successive turns in a scroll. It turns out that both cases occur.

If the change is continuous, the tubule remains circular in cross section and no well defined layer stackings, extending over appreciable volumes, occur.

On the other hand, the change in circumference can be formally accommodated by the insertion of extra material as half-planes parallel to (010), formally associated with edge-type dislocations parallel to the tube axis (Jagodzinski & Kunze, 1954*a*,*b*). The number of unit cells to be inserted per turn is independent of the radius of the tubule and given by $2\pi c/b = 4.98 \simeq 5$ ($t = c$). The strain energy associated with the insertion of 'wedges' or 'half-planes' of extra material will be minimized if the extra material is distributed over as many half-planes as compatible with the structure and if, moreover, the separation of these half-planes is uniform along the periphery. One can

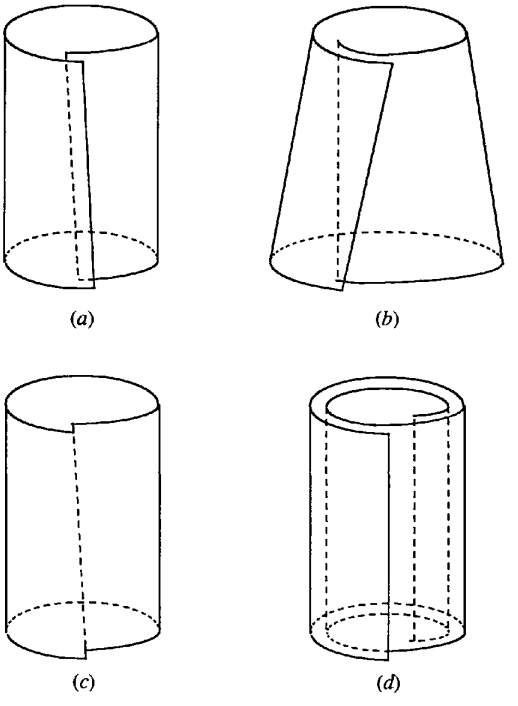

Fig. 2. Different wrapping modes of layers. (*a*) Chiral cylindrical scroll. (*b*) Conically wound scroll. (*c*) Chiral concentric cylinders. (*d*) Cylindrically wound achiral scroll.

distinguish six (010)-type atomic layers in one reference unit cell, which means that supplementary half-planes with a thickness of $\frac{1}{6}b$ are the obvious units of extra material that can be considered (Fig. 1, top).

In terms of dislocation language, one can associate each half-plane with a dislocation parallel to [100] and having a Burgers vector with an edge component $b_e = \frac{1}{6}[010]$. Formally, one would thus need in each turn $6 \times 5 = 30$ edge dislocations. The stable configuration of parallel edge dislocations with the same Burgers vector is a symmetrical tilt boundary of which the tilt angle θ is given by $2 \sin \theta/2 = b_e/D$, where b_e is the edge component of the Burgers vector of the dislocations and D their separation. In the present case, one has $D = c$ and hence $\theta \simeq \arcsin(b/6c) = 12°$, which is consistent with the presence of 30 radial dislocation walls. According to this model, the tubule will thus be divided into 30 wedge-shaped sectors containing planar layers and separated by tilt boundaries in radial planes consisting of partial dislocations with $b_e = \frac{1}{6}[010]$; such tubules do exist and are referred to as 'polygonal serpentine'.

It should be noted that the use of discrete dislocation language is in fact questionable since the separation D of the dislocations is so small that the dislocation cores (of which the separation is c) overlap; the sector walls have, in fact, more the character of grain boundaries. This is the reason why individual dislocations are not observed in the walls (Fig. 3). Formally, one can nevertheless continue to use dislocation concepts and relate the proposed partial dislocations to the atomic structure of serpentine.

The contact layers between successive bilayered 1:1 lamellae are represented schematically in Fig. 1. The large circles represent the limiting layer of OH ions of the close-packed 'brucite' lamella; the small circles are O ions limiting the Si_2O_5 lamella. The translation symmetry of the contact configuration, as suggested by the simplest $1T$ stacking, is given by the unit mesh outlined in Fig. 1 ($a = 0.52$, $b = 0.92$ nm): it is C-centered orthorhombic, quasi-hexagonal. A particular stacking of the two lamellae can be characterized by the positions of the centres C of the SiO_4 hexagonal rings, marked by crosses in Fig. 1. The bonding (hydrogen bonds) between these two layers is assumed to be the weakest and shear associated with disorder may thus take place between these layers. In describing subsequently imaginary shear processes, we assume the OH layers to remain stationary whilst the O layer moves.

When considering only the two layers represented in Fig. 1, all configurations in which the crosses occupy the centres of a triangle of OH ions are symmetry related and energetically equivalent. The difference in energy between different stacking modes obeying these rules must be very small. A succession of the relative positions realized on shearing the two layers can now be specified unambiguously by giving the path followed by a point such as C along the centres of triangles of OH ions. Possible glide paths using such low-energy intermediate positions are indicated in Fig. 1. The bending axis (*i.e.* the fibre axis) is assumed to be perpendicular to the resultant shear direction. The shear along [010] is likely to take place in six partial steps according to the scheme

$$[010] = \{\tfrac{1}{6}[\bar{1}10] + \tfrac{1}{6}[110]\} \times 3. \qquad (1a)$$

In each of these steps, an energy barrier has to be overcome since two of the six O ions in an SiO_4 ring have to 'pass over' OH ions (see, for instance, the motion $A \rightarrow A'$ in Fig. 1).

Since the (001) plane is centred, $\frac{1}{2}[110]$ is a symmetry translation and only three steps,

$$\tfrac{1}{6}[110] \times 3, \qquad (1b)$$

are required to reach a crystallographically equivalent position along [110]. Again, similar energy barriers have to be overcome; moreover, faults with respect to the $1T$ structure in which the central cross of a ring occupies an OH site are present. However, this should be a low-energy fault.

The energy barrier mentioned above can be avoided for shear along [010] if the dissociation takes place in three steps only:

$$[010] = \tfrac{1}{3}[010] \times 3 \qquad (2)$$

[marked by (c) in Fig. 1]. The O ions now 'pass by' the OH ions instead of 'passing over' the top. Reasoning in terms of dislocations, one can see that energy may be gained by dissociation into six partial steps as compared with the three-step process but only at the expense of having to overcome an energy barrier.

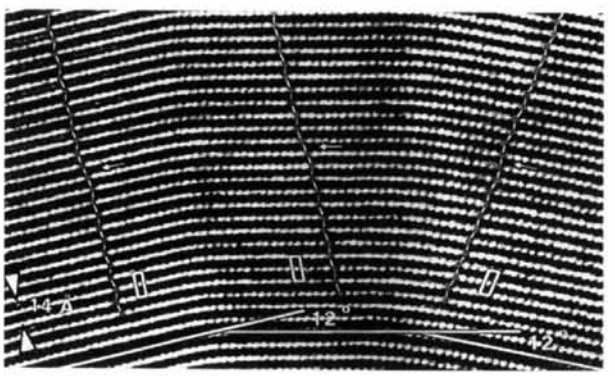

Fig. 3. High-resolution image parallel to the fibre axis of a polygonal serpentine. A change in stacking, which can be described as a homogeneous shear, occurs at each sector boundary. Note that a stacking fault (indicated by an arrow) is transmitted through the sector boundaries.

Subtle kinetic reasons related to the growth conditions may therefore favour one or other dissociation scheme, especially since hydrogen bonds O···HO have to be broken and remade during a real shear process. Similar 'dissociation' schemes have been discussed by Devouard & Baronnet, 1996).

Homogeneous shear according to scheme (2) (Fig. 1*c*) gives rise to an orientation difference of 24° across sector boundaries and thus leads to 15-sector polygonal fibres.

Since the shear process is a consequence of the stresses associated with the bending, one would expect a preference for scheme (1*b*) in parachrysotile and for schemes (1*a*) and (2) in orthochrysotile.

In the case of scheme (1*b*), the orientation change θ across a sector boundary would become $\theta = (b/3 \times 3^{1/2})/c = 14$–$15°$, *i.e.* the fibre would contain 24 sectors when polygonized. This suggests that, whereas polygonal chrysotile-type serpentines may contain either 15 or 30 sectors, polygonal parachrysotile would contain 24 sectors.

Next to the simple schemes considered so far, the homogeneous shear may take place according to more complicated glide paths. This would be the case in chiral tubes where the fibre axis and hence also the shear stresses have a complicated direction.

The fourfold glide path for $\frac{1}{2}[110]$ represented in Fig. 1(*d*) allows avoidance of the stacking faults occurring in scheme (1*b*) and could produce the same total curvature, although two different kinds of sector wall would alternate.

The structures in adjacent sectors are clearly continuous along **c** layer planes (Fig. 3) and the high-resolution contrast suggests that the polarity is conserved across the sector walls. The change in stacking requires the passage of one such partial dislocation between *each* successive pair of bilayers. Such a process causes a homogeneous shear over an angle $\theta = \arctan(\frac{1}{6}b/c) \simeq 12°$ {or $\theta = \arctan(\frac{1}{3}b/c) = 24°$}, which thus produces the required orientation difference.

The high-resolution images (Fig. 3) along [010] are compatible with both types of dissociation since they only reveal the homogeneous shear.

Even if the stacking changes continuously, the same stacking pattern will nevertheless repeat after an azimuth increase of 72° (*i.e.* $6 \times 12°$ or $3 \times 24°$). Thus, if a given reference crystallographic stacking occurs along a certain radial direction, this will repeat five times along the periphery, *i.e.* the fibre has fivefold rotation symmetry (Baronnet & Mellini, 1992; Cressley & Whittaker, 1993; Baronnet, Mellini & Devouard, 1994). In view of the low stacking-fault energy, the stacking will mostly be complicated or even random along any radial direction unless the fibre is a scroll rather than a set of concentric cylinders.

3. Experimental

3.1. *Materials*

We discuss observations on three types of sample: two natural ones and a synthetic one. The emphasis is on the interpretation of the electron diffraction patterns obtained from individual fibres of such samples. In particular, the diffraction features associated with conically wound fibres will be discussed in detail. The samples are described by Devouard (1996).

3.2. *Specimen preparation*

Samples suitable for transmission electron microscopy were made from the natural samples by ion-beam thinning of slices cut perpendicular to the fibre bundles. Such samples were suitable for observations with the electron beam along the fibre axis.

Since the synthetic sample consisted of separate fibres, specimens were prepared by the evaporation of a drop of distilled water with fibres in suspension on a copper grid covered with a holey carbon film. The latter specimens were suitable for observations with the electron beam perpendicular to the fibre axis. Useable specimens were invariably rather thick, the thinner parts being almost instantly damaged by irradiation. Diffraction patterns and the corresponding images were obtained partly with a JEM 2000 microscope operated at 200 kV (at the CRMC2-CNRS facility, Marseille) and partly with a JEOL 4000 and a Philips CM-20 microscope, operated at 400 and 200 kV, respectively (at EMAT, Antwerp).

4. Description of observed diffraction patterns

In this section, we limit ourselves to a description of the main diffraction effects; a more rigorous formulation and interpretation follow.

4.1. *Zone parallel to the fibre axis*

Along the [100] zone, *i.e.* parallel to the axis of a cylindrical orthochrysotile fibre, the diffraction pattern consists of circular loci centred on the origin of reciprocal space, resembling in many respects a Debye–Scherrer powder pattern. Unfortunately, no diffraction patterns could be obtained from circular fibres owing to their small size. However, the diffraction patterns in this zone axis can be simulated (Whittaker, 1955*b*; Devouard & Baronnet, 1996) or investigated by optical or numerical Fourier transformation of high-resolution images (Devouard & Baronnet, 1996). Polygonized serpentines have larger sizes and did produce [100] zone patterns. This zone reveals the polygonal character of the fibre, if present, as for instance in Fig. 4. It is clear that the circles corresponding to $00l$ reflections ($l = 1, \ldots, 6$) exhibit 30 reinforcements corresponding to the 30 sectors of the

polygonal cylindrical fibre. All reinforcements in successive 'circles' are aligned along radial directions perpendicular to the facets of the polygonal fibre.

The slightly polygonal circles corresponding to $0k0$ reflections ($k = 2, 4$) are diffuse in that they are in fact formed by streaks tangent to these 'circles'. The streaks are a consequence of the disorder in the stacking of (001) layers. Such disorder is not revealed in the $00l$ reflections but causes streaking of $0kl$ reflections. Whereas the 020 and 040 circles are formed by tangent streaks, the 060 circle consists of unstreaked spots. This suggests that the defects responsible for the streaks are faults on (001) with a displacement vector of the type $\mathbf{R} = \frac{1}{6}[x10]$ with respect to the reference structure. The dot product $\mathbf{g} \cdot \mathbf{R}$ is then fractional except for $g = [0k0]$, $k =$ multiple of 6. Faults with a displacement vector $\mathbf{R}$ are not revealed by reflections with a diffraction vector $\mathbf{g}$ such that $\mathbf{g} \cdot \mathbf{R}$ is an integer. It is also consistent with the fact that k has to be even and at the same time a multiple of three to exhibit sharp $0kl$ spots. The latter condition arises because the MgOOH octahedra sublattice remains invariant under displacements along [010] associated with low-energy stacking faults.

No diffraction patterns of conical fibres along the fibre axis have been obtained so far.

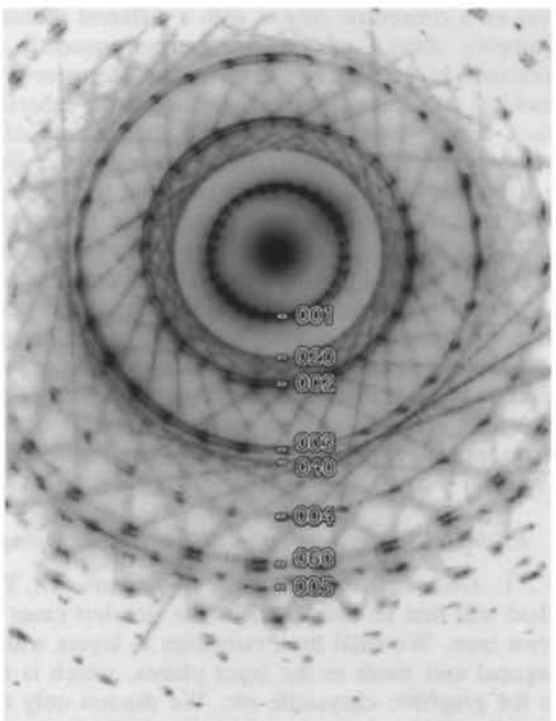

Fig. 4. Diffraction pattern along the $[100]_0$ zone fibre axis of a 30-sector polygonal serpentine fibre. The circles of spots are split along radial directions (possibly due to refraction). The 020 and 040 circles are formed by tangent streaks along $\mathbf{c}^*$ where the 060 circle consists of sharp spots.

4.2. *Quasi-normal incidence*

4.2.1. *The 00l reflections.* Observations on cylindrically wound fibres have been described in detail for carbon nanotubes (Zhang *et al.*, 1994); they are similar in cylindrical serpentines.

In the diffraction pattern under close to normal incidence, the main intense spots produced by conical fibres consist of two equispaced linear arrays of relatively sharp spots, intersecting at the origin under an angle equal to the projected apex angle of the cone. The configuration of the two arrays has only one line of symmetry, the two arrays being shifted in opposite sense along their length with respect to the origin. The line of symmetry is parallel to the fibre axis. This surprising phenomenon was noted earlier (Yada, 1967, 1971) and correctly attributed to 'refraction' of the electrons that traverse the specimen under grazing incidence close to the fibre surfaces. For a cylindrical specimen, refraction only gives rise to spreading or possibly doubling of the $00l$ reflections along $\mathbf{c}^*$, but in

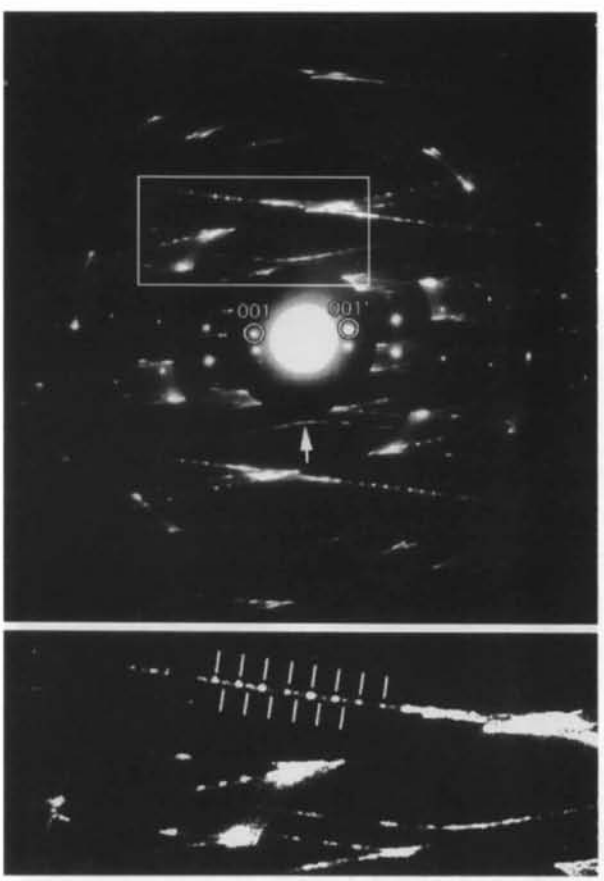

Fig. 5. Diffraction pattern of a conical fibre. The beam is incident roughly perpendicular to the fibre axis. The cone angle is $2\phi_0 = 19$–$20°$. Note the presence of V-shaped streaks attached to all spots (except the $00l$ spots) and of broad curved streaks connecting two spots on the same circle. Note the presence of the superstructure spots shown magnified on the inset.

a conical fibre it leads to two differently oriented linear arrays, each perpendicular to one of the projections of the 'walls' (see Fig. 9*a*).

4.2.2. *Superperiod reflections: streaks.* A second striking feature is the presence of closely spaced spot arrays along lines parallel to the two c^* directions and passing through *hkl* diffraction spots. These arrays of spots suggest the presence of a superperiod along the c^* direction. All spots, except the sharp 00*l*-type spot sequences, acquire *V*-shaped streaks extending away from the fibre axis along directions parallel to the 00*l* rows of spots. The streaks are sometimes rather continuous with reinforcements but they often exhibit sharp equidistant spots. Some of the streaks have the shape of one branch of a hyperbola having the straight streaks as asymptotes.

4.2.3. *The hkl reflections.* Most striking is the absence of a clear geometrical pattern for most zone axes; in particular, the spots do not form a regular hexagon. There is only a centre of symmetry for the configuration of this type of reflection. In certain zone patterns, pairs of spots on the same circle are connected by wide curved streaks (Fig. 5). Most diffraction patterns contain only a small number of spots for each spatial frequency. We shall see that this is a consequence of the symmetry of the arrangement of reciprocal-space loci for particular cone angles. The density of spots along a given circle depends sensitively on the semi-apex angle ϕ_0 as deduced from the angle enclosed by 00*l* rows, as for instance in Fig. 6 where $\phi \simeq 5°$.

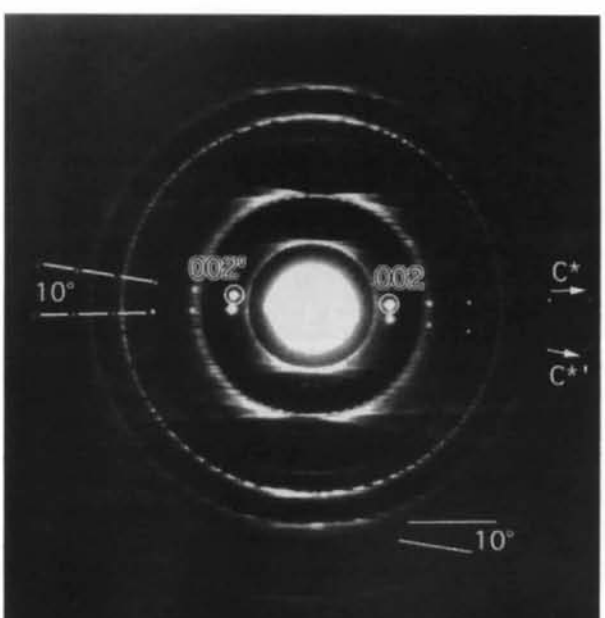

Fig. 6. Electron diffraction pattern of a conical fibre with a cone angle $2\phi_0 = 10°$. Note the large concentration of streaked spots along the successive circles of constant spatial frequency, consistent with the small cone angle.

5. Methods to describe the geometry of diffraction space of rolled microstructures

5.1. *Spherical coordinates, cylindrical projection*

A discussion of the diffraction space of rolled textures such as cylindrically or conically wound layered microstructures can conveniently be based on a spherical coordinate reference system because all reciprocal-space nodes referring to a family of lattice planes with the same local interplanar distance are situated on a sphere with radius $R = g_{hkl} = 1/d_{hkl}$, whatever the geometry of the rolled microstructure.

The coordinates of a point on the sphere will be called α (the latitude) and ψ (the azimuth or longitude) (Fig. 7*b*), and R is the radius of the sphere. A reciprocal-lattice node (ψ, α) will become stretched out over a line locus situated on the sphere. The shape of this locus with equation $F(\psi, \alpha) = 0$ depends on the geometry and on the symmetry of the wrapping and, as we shall see, it may become a complex three-dimensional curve such as a spherical spiral. In general, each node with a given d_{hkl} produces a separate curve on the sphere with radius g_{hkl}, leading to a complex geometry. Families of nodes with a different d_{hkl} will produce similarly complex curves on a concentric sphere with a different radius.

Complex curves on a sphere can subsequently be represented in the plane by the use of a Mercator-type cylindrical projection (Fig. 8*a*). A point on the spherical surface is therefore projected onto the surface of a circular cylinder with generators parallel to the fibre axis, which is tangent to the sphere along the equator. Unrolling this cylinder produces a planar representation. The latitude α is plotted either as $\sin\alpha$ (in Fig. 8*b*) or as α itself vertically along the y axis and the longitude ψ is plotted along the horizontal axis in the manner used for geographical maps. However, in the present application to spherical spirals, ψ may extend over several turns. It is therefore meaningful to consider the cylinder as a scroll so that the function $F(\psi, \alpha) = 0$ remains single valued. The latitudes α are restricted to the interval $-\pi/2 \leq \alpha \leq +\pi/2$.

5.2. *Examples of application to cylindrical wrappings*

5.2.1. *Geometrical description of the patterns.* The method will first be illustrated by the simplest cases of interest here. We shall limit ourselves to layers with a hexagonal unit mesh in the layer planes, which is the case for graphite, chrysotile *etc.* We discuss only the pattern formed by the nodes of the first hexagon (*i.e.* of the type $10\bar{1}0$ in hexagonal notation). A similar discussion is applicable to the nodes of the second hexagon (*i.e.* of $11\bar{2}0$ type) and higher-order hexagons. We also limit ourselves to the geometry of the patterns,

since in electron diffraction spot intensities are dynamical and depend on many parameters.

The $00l$ loci form a singular case because they are not sensitive to one-dimensional stacking (or orientational) disorder along the c direction. These loci remain sharp circles in planes normal to the fibre axis in all considered cases.

The parameter ψ only plays a role if the diffraction space no longer has cylindrical symmetry, as in the case of conically wound scrolls, but in most cases the cylinder symmetry is conserved and two numbers are sufficient to designate a circular locus: the radius R of the sphere, which is equal to the length of the diffraction vector $|\bar{\mathbf{g}}_{hkl}| = g_{hkl}$, and the latitude α on that sphere, the equator being perpendicular to the fibre axis.

As a first example, we discuss orthochrysotile (Fig. 9*a*); the fibre axis is along [100], which is also a twofold axis for the lattice (not for the structure!) and the situation is degenerate, *i.e.* one circle corresponds to two nodes. The main circular loci (and points) are now given by

$$\alpha_{110} = 60°; \quad R = g_{110},\ g_{220}, \ldots$$
$$\alpha_{110} = -60°; \quad R = g_{110}, g_{220}, \ldots$$
$$\alpha_{111} = 0; \quad R = g_{110}, \ldots$$
$$\alpha_{00l} = 0; \quad R = g_{00l}\ (l = \pm 1, \pm 2, \ldots)$$
$$\alpha_{0k0} = 0; \quad R = g_{0k0}\ (k = \pm 2, \pm 4, \ldots),$$

where g_{hkl} is given by the expression

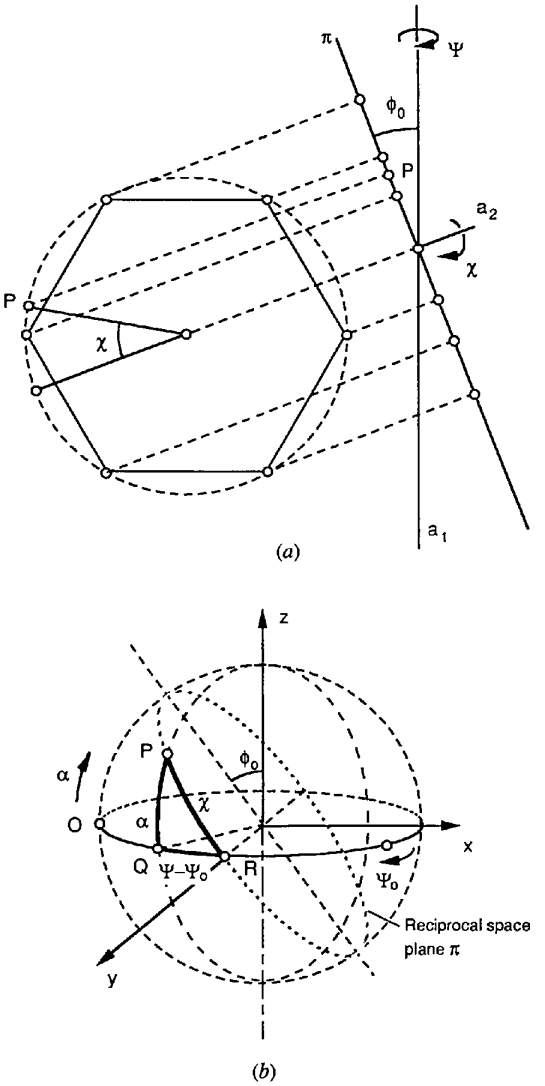

Fig. 7. Construction of diffraction loci. (*a*) The diffraction locus corresponding to a reciprocal-lattice node P, for a conical fibre, is obtained by the coupled rotation of the plane π about the axis a_1 parallel to the fibre axis (rotation angle described by ψ) and of the node configuration in π about the axis a_2 perpendicular to π (described by χ); ϕ_0 is the semi-apex angle of the cone. Two projections are shown. (*b*) Reference system (ψ, α) used in describing diffraction space; ψ is the azimuth and α the latitude; ϕ_0 is the semi-apex angle of the cone. The angle χ refers to the point P along the large circle.

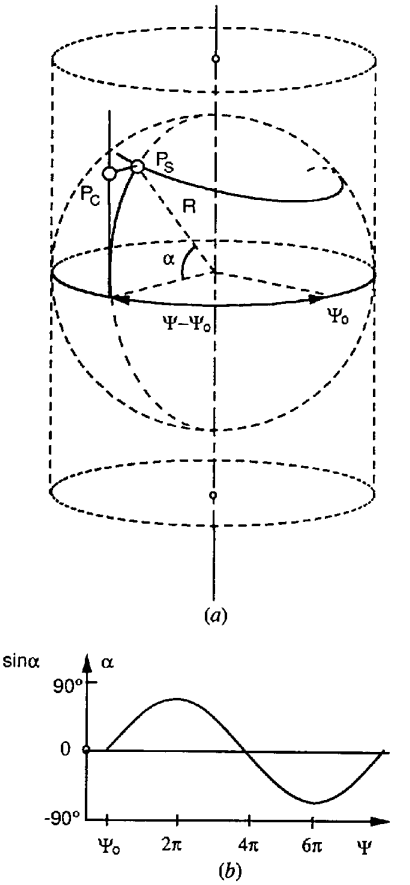

Fig. 8. (*a*) Mercator-like cylindrical projection used to represent spherical spiral loci in a plane. The point P_s on the sphere at (ψ, α) projects in the point P_c $(\psi, \sin\alpha)$ on the cylindrical scroll tangent to the sphere. (*b*) When unrolling the cylindrical scroll, the projection of the spherical spiral is a sinusoid.

$$R = g_{hkl} = [(ha^*)^2 + (kb^*)^2 + (lc^*)^2]^{1/2}. \quad (3)$$

Apart from 001, we do not consider here loci with $l \neq 0$.

Intersections with the Ewald plane can easily be obtained. If the incident beam is parallel to the fibre axis, the loci with $\alpha = 0$ will be excited. If the incident beam is perpendicular to the fibre axis, the Ewald plane intersects along a plane $\psi =$ constant. In the cases considered as yet, the intersection pattern is independent of ψ.

As a second example, we discuss parachrysotile (Fig. 9*b*), for which the fibre axis is [010]; the unit mesh in the planes tangent to the cylinder $a = 0.52$, $b = 0.92$ nm such that $\arctan(a/b) \simeq 30°$. The fibre axis is a twofold symmetry axis of the lattice. The situation is again said to be 'degenerate' since symmetry-related pairs of reciprocal-lattice nodes lead to only one circle. The main features of diffraction space are then given by the following circles characterized by (α, R):

$$\begin{aligned}
&\alpha_{110} = 30°; && R = g_{110}, g_{220}, \ldots \\
&\alpha_{110} = -30°; && R = g_{110}, g_{220}, \ldots \\
&\alpha_{110} = 90°; && R = g_{110}, \ldots \\
&\alpha_{110} = -90°; && R = g_{110}, \ldots \\
&\alpha_{00l} = 0; && R = g_{00l}\ (l = \pm 1, \pm 2, \ldots) \\
&\alpha_{0k0} = 0; && R = g_{0k0}\ (k = \pm 2, \pm 4, \ldots).
\end{aligned}$$

The circles in $\alpha = \pm 90°$ are clearly degenerated into points. The diffuse character of some of these loci will be discussed later.

In chiral cylindrical tubules or scrolls, the degeneracy is lifted and single circles associated with pairs of symmetry-related nodes split into two parallel circles on the same sphere but with α values given by $\alpha + \eta$ and $\alpha - \eta$, where α is the latitude in the achiral case and 2η is the chiral angle. Note that *no* splitting takes place for circles generated by nodes corresponding to the set of planes tangent to the cylinder (Fig. 9*c*).

Clinochrysotile is monoclinic with a β angle close to 90° (mostly 93°) (Fig. 9*d*). The c^* and b^* directions are still perpendicular to the fibre axis but $\mathbf{a}^*$ is no longer parallel to it. As a result, the nodes $h0l$ describe two concentric circular loci. The main set of circular loci is now given by

$h0l$

$$|\bar{g}_{h0l}| = [(ha^*)^2 + (lc^*)^2 + 2hla^*c^* \cos\beta]^{1/2}$$
$$\alpha_{h0l} = \arctan[(ha^* \sin\beta + lc^*)/(-ha^* \cos\beta + lc^*)] \quad (h \text{ even})$$

$hk0$

$$|\bar{g}_{hk0}| = [(ha^*)^2 + (kb^*)^2]^{1/2}$$
$$\alpha_{hk0} = \arctan(ha^*/kb^*)$$

$00l$

$$|\bar{g}_{00l}| = lc^*$$
$$\alpha_{00l} = 0$$

$0k0$

$$|\bar{g}_{0k0}| = kb^* \quad (k \text{ even})$$
$$\alpha_{0k0} = 0.$$

In cylindrical fibres, the c-layer stacking often exhibits appreciable disorder and therefore the $hk0$ and $0k0$ spots are mostly streaked along the c^* direction, *i.e.* tangent to the circular loci. The $0k0$ and $hk0$ circular loci can therefore be described as intensity discs that are sharply limited inwards by the described circles but fade out outwards (Amelinckx *et al.*, 1994, 1995; Liu & Cowley, 1994*a*,*b*; Baker, 1989; Tibbets, 1984). Inter-

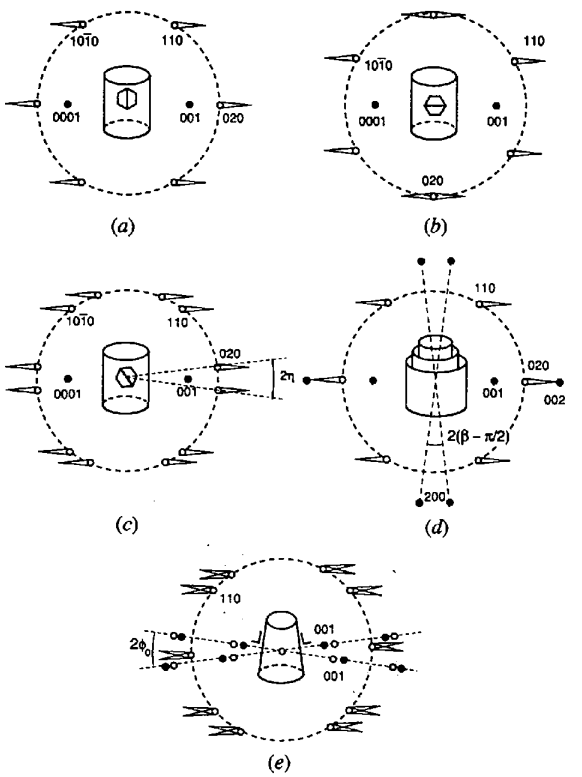

Fig. 9. Schematic representation of different types of fibre diffraction pattern. The wrapped layers are referred to a hexagonal unit mesh, indicated schematically. In all cases, the fibre axis is vertical. Only spots of the first order, *i.e.* of the type 10$\bar{1}$0 in the hexagonal description (or 110 and 020 in the orthorhombic description), are indicated. (*a*) Cylindrical fibre: axis parallel to [10$\bar{1}$0] (or [001] – orthochrysotile type). (*b*) Cylindrical fibre: axis parallel to [11$\bar{2}$0] (or [010] – parachrysotile type). (*c*) Helically wound cylindrical fibre. (*d*) Clinochrysotile type. Note the splitting of the 200 reflections owing to the monoclinic symmetry. (*e*) Conically wound cylindrical fibre. Note the splitting of the [00*l*] directions. The streaked spots are located on the 110 circle. The full dots indicate the actual spot positions 00*l* after refraction.

section with a plane ψ = constant (Ewald's sphere for normal incidence) then leads to diffraction spots streaked towards high spatial frequencies but sharply limited inwards. These discs or coronae can be obtained by the rotation about the fibre axis of a diffuse line parallel to $\mathbf{c}^*$ through $hk0$ and which is tangent to the $hk0$ loci. In nodes situated on the projection of the fibre axis, the two line segments join into a single diffuse line parallel to $\mathbf{c}^*$, the inner circle being shrunk to a point (Fig. 9*b*).

In the diffraction pattern of cylindrical fibres, the reflections of type $h0l$ and $hk0$ are situated in positions that are related by a line of symmetry parallel to the projection of the fibre axis, the overall planar symmetry of the pattern being $mm2$. This still applies if the fibre axis is not normal to the incident beam and even if the fibre is chiral (Zhang *et al.*, 1994; Chisholm, 1988). This is no longer the case in conical scrolls, as in Fig. 10, which will be discussed in more detail below.

5.2.2. *Observations on cylindrical chrysotile.* The theoretical patterns of Fig. 9 will now be compared with experimental patterns; first for cylindrical fibres.

The diffraction pattern reproduced in Fig. 11 can be compared with the predicted pattern of Fig. 9(*d*); it shows that the fibre is clinochrysotile with a β angle close to 93°.

Fig. 12 shows a single-fibre chrysotile diffraction pattern as viewed along the direction normal to the fibre axis. The repeat distance along the fibre axis, which is vertical in Fig. 12, is b^*, showing that the fibre is parachrysotile.

A synthetic chrysotile fibre pattern, the incident beam being quasi-normal to the fibre axis, is reproduced in Fig. 13. The horizontal sequence of sharp $00l$ reflections shows that the fibre axis is vertical in Fig. 13. Doubling of spots other than $00l$ shows that the fibre has chiral character, the chiral angle being close to 7.5°. Note the streaking parallel to $\mathbf{c}^*$ of such reflections.

In Fig. 13, the streaks perpendicular to the fibre axis exhibit striking reinforcements with a period of $\frac{1}{2}c^*$ in positions determined by basic spots of the second and fourth hexagons. Since the basic spots that determine these positions are not separated by a distance that is simply related to c^*, two interleaved sequences with a spacing $\frac{1}{2}c^*$ result. This observation suggests that this fibre has a layer spacing of $2c$ (~ 14 Å). Moreover, the fibre was presumably a scroll since the stacking is repeated with a rather well defined period of $2c$. The

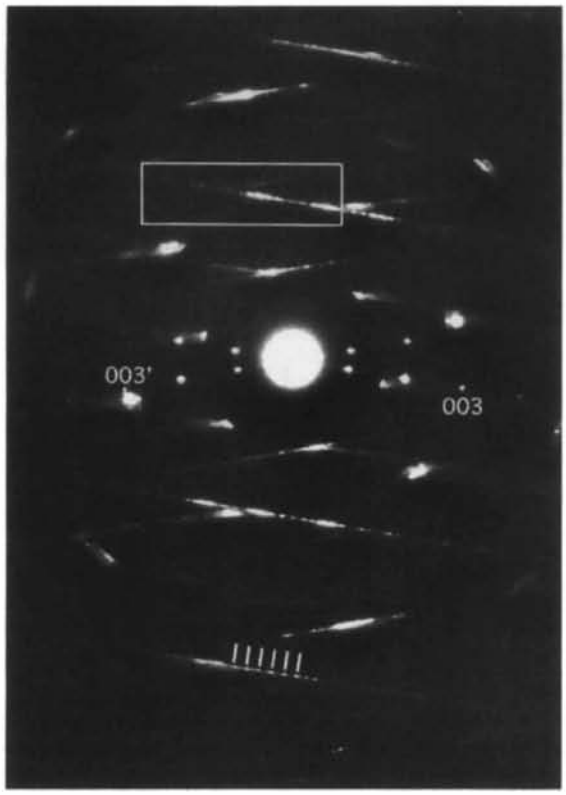

Fig. 10. Electron diffraction pattern of a synthetic conical fibre. Note the lack of $mm2$ symmetry. Note also the *V*-shaped streaks, some of which exhibit sharp reinforcements corresponding to a period $6c$. The cone angle is $2\phi_0 \simeq 19$–$20°$.

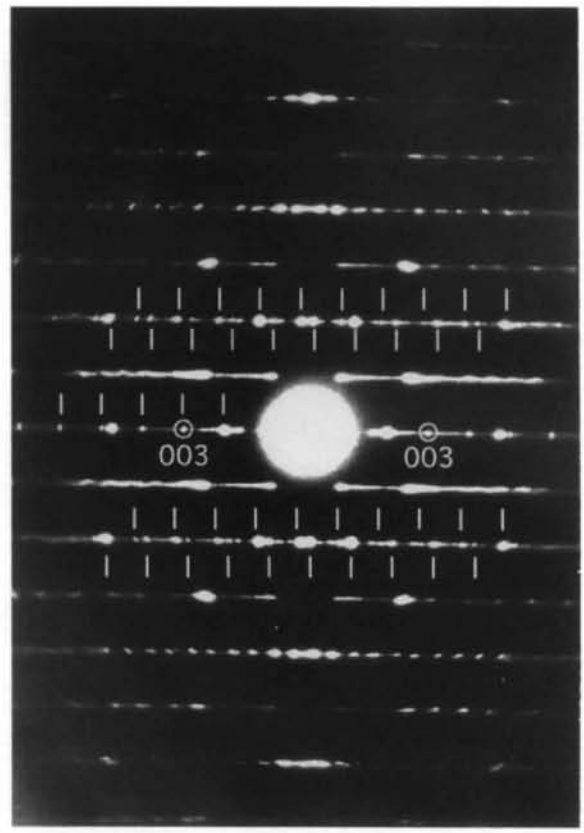

Fig. 11. Diffraction pattern of clinochrysotile under quasi-normal incidence of the beam.

pattern is thus consistent with the wrapping of a two-layer chiral scroll.

5.3. *Ewald plane in spherical coordinates*

The Ewald plane intersects the projection sphere along a large circle (Ewald circle). If γ is the tilt angle, *i.e.* the angle enclosed by the beam direction and the plane normal to the fibre axis, the following relation has to be satisfied along the Ewald circle (in the spherical triangle *PQR*, Fig. 14):

$$\tan\alpha = \operatorname{cotan}\gamma \sin(\psi - \psi_{0,E}). \tag{4}$$

This is in a sense the equation in spherical coordinates of the Ewald circle. If the origin of the azimuth is chosen such that $\psi - \psi_{0,E} = 0$ for $\alpha = 0$, this reduces to

$$\tan\alpha = \operatorname{cotan}\gamma \sin\psi. \tag{5}$$

This choice is always possible in the case where diffraction space has cylindrical symmetry since then the intersections do not depend on ψ. In cases where α depends on ψ, the choice of origin must be the same for diffraction space and for the Ewald circle and in general we will have $\psi_{0,E} \neq 0$ if the Ewald plane is not in a symmetry orientation.

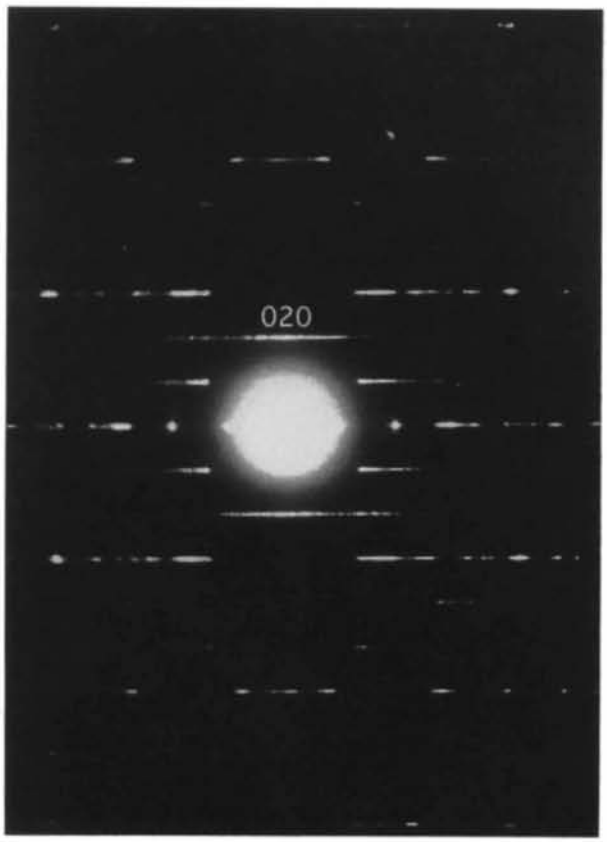

Fig. 12. Diffraction pattern of parachrysotile fibre under normal incidence of the beam.

The quantity of direct interest for comparison with the observed diffraction pattern is the angle χ_E, which is measured directly on the diffraction pattern (Fig. 14). This angle χ_E is related to α by the relation

$$\sin\alpha = \sin\chi_E \cos\gamma. \tag{6}$$

If the beam is incident along the fibre axis, $\gamma = 90°$ and hence $\sin\alpha = 0$. The diffraction spots are then found by putting $\alpha = 0$ since they are the intersection points of diffraction space with the equatorial plane. If the beam

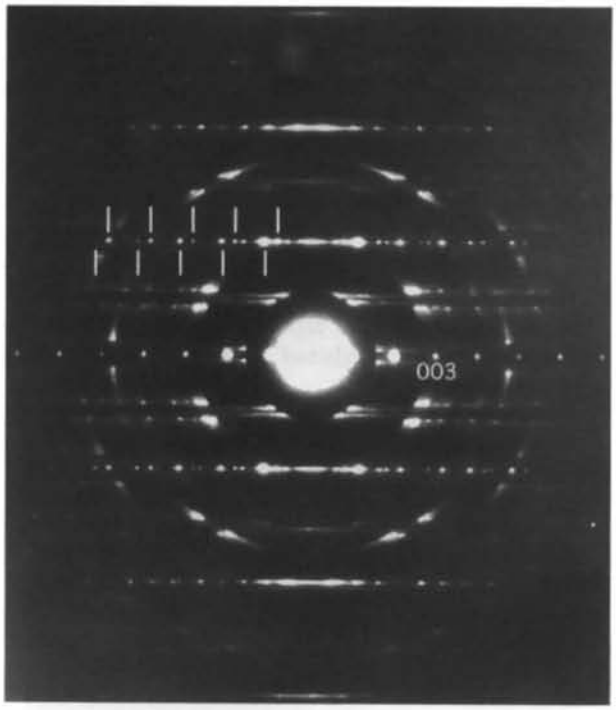

Fig. 13. Diffraction pattern of chiral cylindrical tubule of synthetic chrysotile fibre. The chiral angle $\eta \simeq 7.5°$.

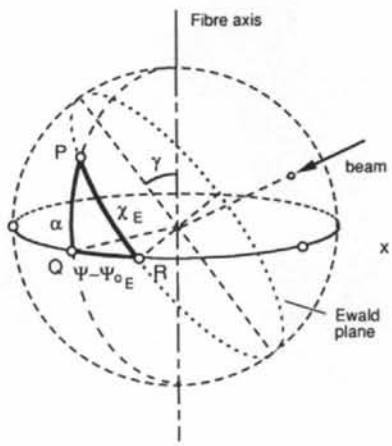

Fig. 14. Reference system used to describe the Ewald plane in spherical coordinates; γ is the angle of incidence of the beam: $\gamma = 0$ for normal incidence, $\gamma = 90°$ for incidence along the fibre axis. The parameters γ and $\psi_{0,E}$ determine the Ewald plane.

is incident along a normal to the fibre axis, $\gamma = 0$ and one has $\alpha_n = \chi_{n,E}$. The angular positions $\chi_{n,E}$ of the diffraction spots are then the α_n. For an arbitrary incidence, (6) gives the observed angle $\chi_{n,E}$ in terms of the angles α_n defining the loci.

The two intersection points of a given circular locus with the Ewald plane will coincide for a critical inclination γ_c, whereby the Ewald plane is tangent to the cone corresponding with the given locus α_n, *i.e.* for $\gamma_c = \pi/2 - \alpha_n$.

5.4. *The effect of polygonization on the reciprocal space of cylindrical fibres*

It was shown that cylindrical serpentine fibres can have a polygonal cross section (Middleton & Whittaker, 1976), *i.e.* they consist of a number (15 or 30) of wedge-shaped sectors separated by planar radial boundaries. Within the sectors, the c layers are planar and parallel to the facets, whereas a localized homogeneous shear, with a component $\frac{1}{6}\mathbf{b}$ (or $\frac{1}{3}\mathbf{b}$) parallel to $\mathbf{b}$, takes place across the boundaries, changing the stacking in successive sectors since the shear vector is not a symmetry translation.

The effect of polygonization on diffraction space is to cause reinforcements in the $0kl$ and $00l$ circles along directions normal to the facets of the fibres. Since the stacking of bilayers within the sectors often exhibits disorder, streaks parallel to $\mathbf{c}^*$ are caused through $0kl$ positions ($k = 2, 4, 6, \ldots$). All these features are revealed in the [100] zone pattern of Fig. 4. The dotted circles at $\alpha = 0$ (in the equatorial plane) are visible because, owing to the thin nature of the specimen, they are in fact circular bands with a certain width normal to the foil, *i.e.* parallel to the fibre axis; relrods are associated with the reinforcements.

Polygonization has no striking effects on patterns along zones other than [100]; it does not affect the spot positions, only the intensity distribution. If the stacking within the sectors is well ordered, the c^* streaks break up into spots.

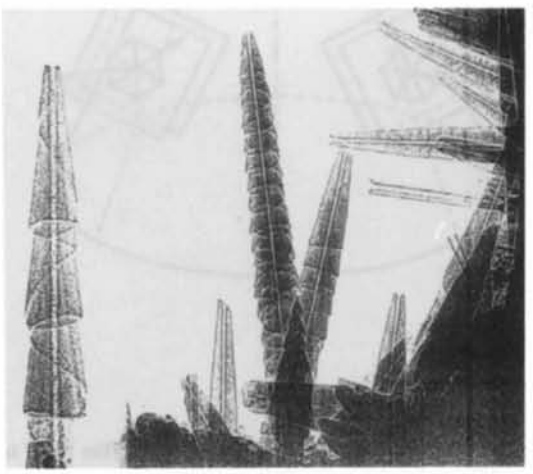

Fig. 15. Transmission-electron-microscope images revealing the concentric cone structure of synthetic chrysotile fibres.

6. Conical wrappings

6.1. *Model of a conical scroll (Amelinckx, Luyten, Krekels, Van Tendeloo & Van Landuyt, 1992; Luyten et al., 1993)*

Conically wound fibres of serpentine are most exceptional in natural samples but are very common in most synthetic samples of chrysotile. They had been recognized as early as 1957 (Zussman *et al.*, 1957) but their complex microstructures are still not fully understood, despite the pioneering work of Yada (Yada, 1967, 1971, 1979; Yada & Iishi, 1977). Although non-scroll conical fibres would be theoretically possible in some cases, most fibres consist of conical scrolls (like a paper cone), as suggested by their morphology (Fig. 15).

In a conical scroll, each sheet is rotated with respect to the adjacent one about an axis parallel to the local normal to the sheet over a constant angle θ, which is directly related to the semi-apex angle ϕ_0 of the cone by the relation (Fig. 16)

$$\theta = 2\pi \sin \phi_0, \tag{7}$$

which is strictly speaking only valid if the sheet thickness Δ is zero.

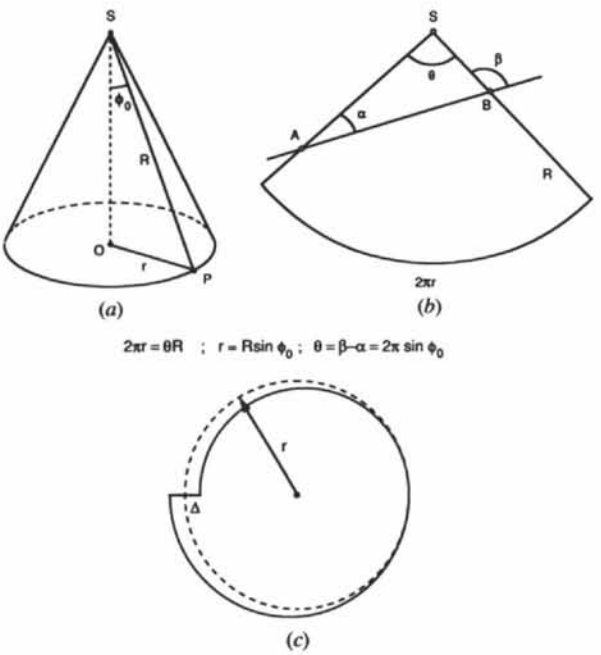

Fig. 16. Illustration of notations used in the derivation of the angular relation between ϕ_0 and θ. (*a*) Geometry of the cone. (*b*) Unrolled cone. (*c*) Relation between turns of an Archimedean spiral (solid line) and circle with the same length (dotted line).

Table 1. *Special values of the semi-apex angle ϕ_0 and of the corresponding θ values $\phi_0 = \arcsin(k/12)$ (k = integer)*

k	θ (°)	ϕ_0 (°)	$N_0 = 1/\sin\phi_0$
1	30	4.78	12
2	60	9.59	6
3	90	14.47	4
4	120	19.47	3
5	150	24.62	2.4
6	180	30	2

If the sheet thickness $\Delta \ll r$ (Fig. 16), which is often the case except perhaps for the first turns of a thick-sheet scroll, (7) is a good approximation, which amounts to assuming that the length of a turn of an Archimedean spiral is equal to the length of a circle with a radius equal to the average radius of curvature of the spiral turn (Fig. 16*c*).

Cone angles tend to adopt certain values for which the successive sheets have a large density of coinciding lattice sites. As a result of the pseudo-hexagonal symmetry of the bilayers, parallel fit occurs for angles that are multiples of 60°; twin-type low-energy interfaces are formed for odd multiples of 30°. The corresponding cone angles ϕ_0 are thus given by

$$\phi_0 = \arcsin(k/12) \quad (k = \text{integer}). \tag{8}$$

The relevant values of ϕ_0 for different values of k are given in Table 1.

A continuum model of a conical scroll is represented in Fig. 2(*b*) and images of such scrolls are reproduced in Fig. 15.

It is geometrically possible to form a concentric conical set of cones (in particular for $\theta = 120°$) but so far there is no evidence for such a stacking mode.

6.2. *Diffraction space of conical wrappings*

A detailed interpretation of the diffraction pattern of conical tubules requires a knowledge of the geometry of diffraction space of such wrappings. We will show that the reciprocal-lattice nodes become either circles or spherical spirals. The diffraction pattern is then the central projection onto the photographic plate of the configuration of intersection points of these curves with the Ewald sphere (plane!).

We assume the cone to have macroscopic rotation symmetry about its axis. The family of *c* planes is tangent to the cone everywhere and the corresponding 00*l* nodes are situated on the normals to these tangent planes. The nodes of type *hk*0 are situated in the plane tangent to the cone. This is shown schematically in Fig. 17 for one position of the tangent planes. Diffraction space is generated by rotating the configuration of *c* planes and nodes about the cone axis, whilst simultaneously rotating the configuration of *hk*0 nodes about an axis normal to the *c* plane through the origin. The two rotations are coupled in the way described above, *i.e.* the *hk*0 node configuration has to rotate over an angle θ for a complete turn of the tangent planes (Fig. 7*a*).

We introduce the azimuth angle ψ characterizing the orientation of the normal to the tangent planes. The orientation of the *hk*0 node configuration within the tangent plane is characterized by the angle χ. An increment in azimuth $d\psi$ causes a change $d\chi$ of the orientation of the *hk*0 node configuration. The two increments are coupled by the relation

$$d\chi = (\theta/2\pi)\, d\psi = \sin\phi_0\, d\psi. \tag{9}$$

This relation is based on the assumption that the orientation change of the *hk*0 configuration, which amounts to θ for an azimuth change of 2π, built up linearly as ψ increases, *i.e.* as the tangent plane rotates. The two angles ϕ_0 and θ are represented in Fig. 7 for a node point $P(hk0)$; it describes a path situated on a sphere with radius g_{hk0}. Integrating (9) and choosing the integration constants such that $\chi = 0$ for $\psi = \psi_0$, one has

$$\chi = (\theta/2\pi)(\psi - \psi_0) = (\psi - \psi_0)\sin\phi_0. \tag{10}$$

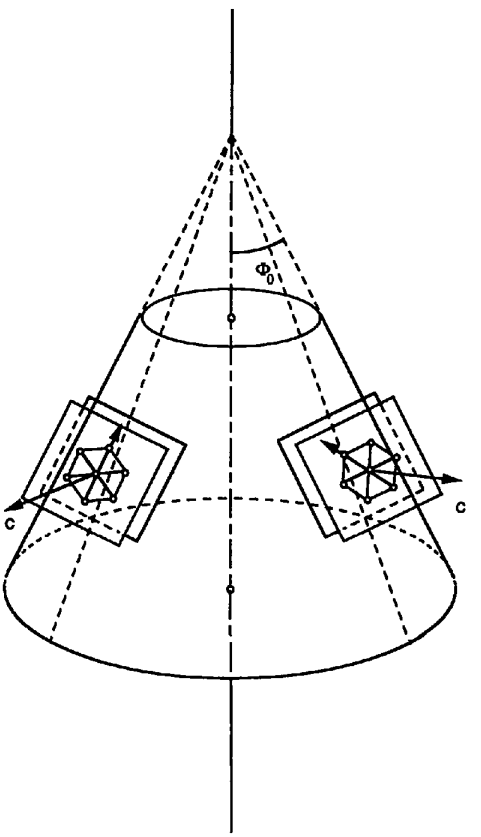

Fig. 17. Diffraction space of conically wound fibre. The set of layer planes (001) is tangent everywhere to a cone with semi-apex angle ϕ_0. The layers are represented by their hexagonal unit mesh; they rotate about the local *c* axis as one describes a path around the axis.

Use is made of spherical coordinates (ψ, α) to describe the locus of P by means of an equation of the type $F(\psi, \alpha) = 0$. In the spherical triangle PQR, one has

$$\sin\alpha = \sin\chi\cos\phi_0. \tag{11}$$

Expressing χ in terms of ψ as in (10), one obtains the locus in the desired form

$$\sin\alpha = \cos\phi_0 \sin[(\sin\phi_0)(\psi - \psi_0)]. \tag{12}$$

Assuming that the reciprocal-lattice nodes $hk0$ form a hexagonal configuration on a circle with radius g_{hk0}, one can describe the loci of this hexagon of nodes as

$$\sin\alpha_n = \cos\phi_0 \sin[(\sin\phi_0)(\psi - \psi_0) + n \times 60°] \tag{13}$$

with $n = 0, 1, \ldots, 5$. This equation represents in general six spherical spirals, one for each node (*i.e.* for each n value) in spherical coordinates. However, as we shall see, symmetry may reduce this number.

The usual coordinate transformation allows one to formulate the equation in terms of Cartesian coordinates:

$$x = g_{hk0}\cos\psi\cos\alpha; \quad y = g_{hk0}\sin\psi\cos\alpha; \quad z = g_{hk0}\sin\alpha. \tag{14}$$

6.3. *The 00l loci*

The loci described by the $00l$ nodes are found by the rotation of the end points of vectors with lengths lc^*, perpendicular to the 'local' c planes, *i.e.* enclosing an angle of $+(\pi/2 - \phi_0)$ or $-(\pi/2 - \phi_0)$ with the rotation axis (Fig. 17). For each l, such a rotation describes a circle with equation $\alpha = \phi_0$ on the sphere with radius lc^*. This set of circles in parallel planes is situated on a rather flat double cone with semi-apex angle $\pi/2 - \phi_0$. The intersections with the Ewald plane under quasi-normal incidence give rise to two sequences of equidistant sharp reflections intersecting in the common origin under an angle $2\phi'$ and shifted longitudinally as a result of refraction. This angle $2\phi'$ is related to the angle $2\phi_0$ but it depends on the inclination of the incident beam. The semi-apex angle ϕ', as observed with the incident beam forming an angle γ with the normal to the cone axis, is related to the semi-apex angle ϕ_0 at normal incidence by the relation

$$\sin\phi' = \sin\phi_0/\cos\gamma. \tag{15}$$

The observed angle ϕ' is thus always larger than the real angle ϕ_0.

When the electron beam is exactly parallel to the cone axis and if the latter is normal to the surfaces, no c reflections are observed unless the angle ϕ_0 is very small and the foil thin so as to produce a sufficiently wide circular band of relrods. In such a case, a circular locus is observed in the [100] zone. For technical reasons, such a diffraction pattern could unfortunately only be obtained from a cylindrical polygonized fibre (Fig. 4). The circles then exhibit reinforcements corresponding to the facets; the latter disappear for a circular cylinder.

When the axis of the cone is inclined with respect to the foil plane, slightly elliptic loci can be produced. The circular locus is now split up into two concentric ellipse-shaped loci, which have a common diameter parallel to the tilt axis of the cone. This common diameter is the long symmetry axis for the inner ellipse and the short symmetry axis for the outer ellipse. The splitting increases linearly with increasing value of l; also, the intensity of the loci becomes weaker with increasing l.

6.4. *Geometrical properties of spherical spirals*

6.4.1. *General aspects.* The shape of one spherical spiral, *i.e.* of the locus of one reciprocal-lattice node, is shown in a stereoview in Fig. 18.

Along a section with the Ewald plane $\psi = 0$ parallel to the cone axis (*i.e.* for perpendicular incidence of the electron beam), the angular separation of two successive intersection points, *i.e.* between successive turns, is given by

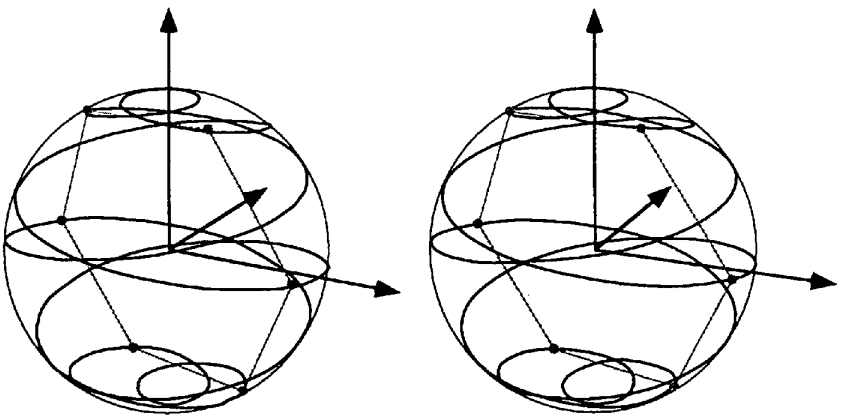

Fig. 18. Spherical spiral representing in a stereoscopic view the locus in diffraction space of a reciprocal-lattice node for a conically wound fibre. The locus is closed ($\theta = 60°$). The curve is tangent to two small circles at a polar distance ϕ_0 around the north and south poles.

$$\Delta\alpha = \arcsin[\cos\phi_0 \sin(2\pi \sin\phi_0)] = \arcsin[\cos\phi_0 \sin\theta]. \quad (16)$$

If ϕ_0 is small enough, $\cos\phi_0 \simeq 1$ and one obtains

$$\Delta\alpha \simeq 2\pi \sin\phi_0 = \theta \quad (17)$$

(ϕ_0 in rad). The density of intersection points decreases with increasing ϕ_0 and with increasing θ.

The extrema, which are equal to $\pm\cos\phi_0$, occur for

$$\psi \sin\phi_0 = k\pi + \pi/2. \quad (18)$$

(k = integer). At these points, the spherical spiral is tangent in the circles $\alpha = \pm(\pi/2 - \phi_0)$.

6.4.2. *Closure condition.* A closed locus will be formed if after an integer number of turns p the corresponding α values are equal and the sine is in the same phase, *i.e.* one must have (for $n = 0$; $\psi_0 = 0$)

$$\psi \sin\phi_0 = (\psi + 2p\pi)\sin\phi_0 \pm 2q\pi \quad (p = \text{integer};\quad q = \text{integer}),$$

i.e. for

$$2p\pi \sin\phi_0 = \pm 2q\pi \quad (19)$$

or, taking (7) into account, for

$$\theta = (2q/p)\pi \quad \text{or} \quad \phi_0 = \arcsin(q/p). \quad (20)$$

θ must thus be rationally related to π or ϕ_0 must have a rational sine. In particular, all 'special' cone angles give rise to commensurate closed loci, as is clear from Table 1.

6.4.3. *Period: number of turns of spiral.* The period of the complete curve is equal to the period of $\sin\alpha$ (12). The period of the sine being 2π, one must have

$$\sin[(\sin\phi_0)\psi + 2\pi] = \sin[(\sin\phi_0)\psi]. \quad (21)$$

This corresponds to a period of $2\pi/\sin\phi_0$ in azimuth, as can be seen by writing

$$\sin[(\sin\phi_0)\psi + 2\pi] = \sin[(\psi + 2\pi/\sin\phi_0)\sin\phi_0]. \quad (22)$$

Since one turn corresponds to a change in ψ of 2π, the number of turns must be

$$N_0 = 1/\sin\phi_0 = 2\pi/\theta, \quad (23)$$

which is only an integer number provided $\phi_0 = \arcsin(1/N)$ (N = integer), which turns out to be the case for all 'special' values of ϕ_0 (see Table 1).

6.4.4. *Extrema of the spherical spiral.* The expression $d\alpha/d\psi$ is a measure of the angle δ under which the tangent to the spherical spiral intersects the equator. From (12), we have

$$d\alpha/d\psi = \tfrac{1}{2}\sin 2\phi_0 \cos[(\sin\phi_0)\psi] \times \{1 - \cos^2\phi_0 \sin^2[(\sin\phi_0)\psi]\}^{-1/2}. \quad (24)$$

At the intersection point of the curve with the equator ($\alpha = 0$, $\psi = 0$), one finds $\tan\delta = \frac{1}{2}\sin 2\phi_0$, *i.e.* $\tan\delta = \phi_0$ for small ϕ_0. As the spiral approaches the poles, this angle decreases monotonously and it becomes zero at the extrema, which are reached for $\cos[(\sin\phi_0)\psi] = 0$, *i.e.* for $\psi\sin\phi_0 = k\pi + \pi/2$; the first one occurs for

$$\psi = \pi/(2\sin\phi_0) \quad (25)$$

(choosing $\psi_0 = 0$ for $\alpha = 0$).

Whenever the diffraction pattern exhibits evidence that the Ewald plane is tangent to the curve (as in Fig. 5), the pattern must have been made under an appreciable inclination angle γ.

6.4.5. *Intersection points with the equator.* The intersection points with the equator are given by $\sin\alpha = 0$ or by

$$\psi = k\pi/\sin\phi_0 \quad (26)$$

(k = integer) with $\psi < 2\pi$. More specifically, for closed curves, $\alpha = 0$; $\psi = kN\pi \pmod{2\pi}$. If N is even, for instance $N = 2m$ ($m \geq 1$, integer), then $\psi = 2km\pi \pmod{2\pi}$. The only acceptable value is $k = 0$ corresponding to $\psi = 0$. The only intersection point is a double point of the curve in the origin of the azimuth. If N is odd, for instance $N = 2m + 1$ ($m \geq 1$), then $\psi = (2m+1)k\pi \pmod{2\pi}$. We now have two different solutions, $k = 0$ leading to $\psi = 0$ and $k = 1$ leading to $\psi = \pi \pmod{2\pi}$. The two intersection points are diametrically opposed and are single points of the curve.

These features are visible in Fig. 19, which represents loci for the remarkable values of ϕ_0 and θ ($\theta = 30, 60, 90, 120, 180°$) corresponding respectively to the number of turns $N = 12, 6, 4, 3, 2$.

Since each turn is at most intersected twice by a plane, the maximum number of intersection points with an Ewald plane is $2N$. This number can be smaller owing to the presence of double points.

6.4.6. *Symmetry of spirals.* The point symmetry of the spiral depends on the parity of N_0. The curves with N_0 even belong to the point group *mm*2, the binary axis passes through the intersection point with the equator, which is a double point. The plane containing the extrema is a mirror plane through the axis: $\psi = \pi/(2\sin\phi_0)$, which coincides with $\psi = 0$ if N_0 is even. The second mirror plane is perpendicular to the fibre axis. There is no centre of symmetry.

The curves with N_0 odd are centrosymmetric; they belong to the point group $2/m$, where the twofold axis passes again through the origin ($\psi = 0$, $\alpha = 0$). The plane containing a double point is still a mirror plane. These properties are suggested by Fig. 19; they can be derived analytically from (12).

The plane through the extrema can be represented as $\psi = \pi/(2\sin\phi_0)$. It is clear that the substitution of ψ by $[\pi/(2\sin\phi_0)] - \psi$ and by $[\pi/(2\sin\phi_0)] + \psi$ leads to the same value of $\sin\alpha$, demonstrating the presence of a mirror plane through the fibre axis. The graphs of Fig. 19 are made as viewed along this mirror plane.

We note that the substitution $\psi \rightarrow \psi + (\pi/\sin\phi_0)$, where $\pi/\sin\phi_0$ corresponds to half a period, leads to the opposite sign for $\sin\alpha$. The conclusions to be drawn from this depend on the parity of $1/\sin\phi_0 = N_0$. If $N_0 = 2k$, this substitution does not change $\psi \pmod{2\pi}$ and the conclusion is that for the same ψ the points $+\alpha$ and $-\alpha$ belong to the curve, which means that there is a mirror plane perpendicular to the axis. If $N_0 = 2k+1$, the substitution replaces ψ by $\psi + \pi \pmod{2\pi}$ and changes α into $-\alpha$. The conclusion now is that the centre of the sphere is an inversion centre for the curve. Since there is already a mirror plane through the axis, the addition of a centre of symmetry implies the presence of a twofold axis through the centre of the sphere and perpendicular to the mirror plane, but no second mirror.

6.4.7. *Closure after a number of turns.* As mentioned above, the condition for closure of the spherical spiral is

$$1/\sin\phi_0 = p/q, \tag{27}$$

where p and q are mutually prime integers.

In the cases considered as yet (Fig. 19), $p = N_0$ (integer, equal to the number of turns) and $q = 1$. The curve contains N_0 full turns and intersects the equator twice, once going northwards and once going southwards. For N_0 even, these two intersection points coincide in a double point; for N_0 odd, both points are single and situated at diametrically opposed points.

Closed curves, which pass more than twice through the equator, can occur if $1/\sin\phi_0$ is not an integer. In the case where $q \neq 1$, the period of $\sin\alpha$ is

$$2\pi(p/q) = 2\pi(N + \varepsilon) \tag{28}$$

($\varepsilon < 1$). It is a non-integral number of turns along the sphere and as a result does not coincide with the period of ψ ($= 2\pi$). The curve will only close if after a 'superperiod' both $\sin\alpha \pmod{2\pi[p/q]}$ and $\psi \pmod{2\pi}$ repeat. This occurs for the smallest common multiple of $2\pi(p/q)$ and 2π, *i.e.* for $2\pi p$. The curve thus closes after p turns. The number of intersection points with the equator is then $2q$.

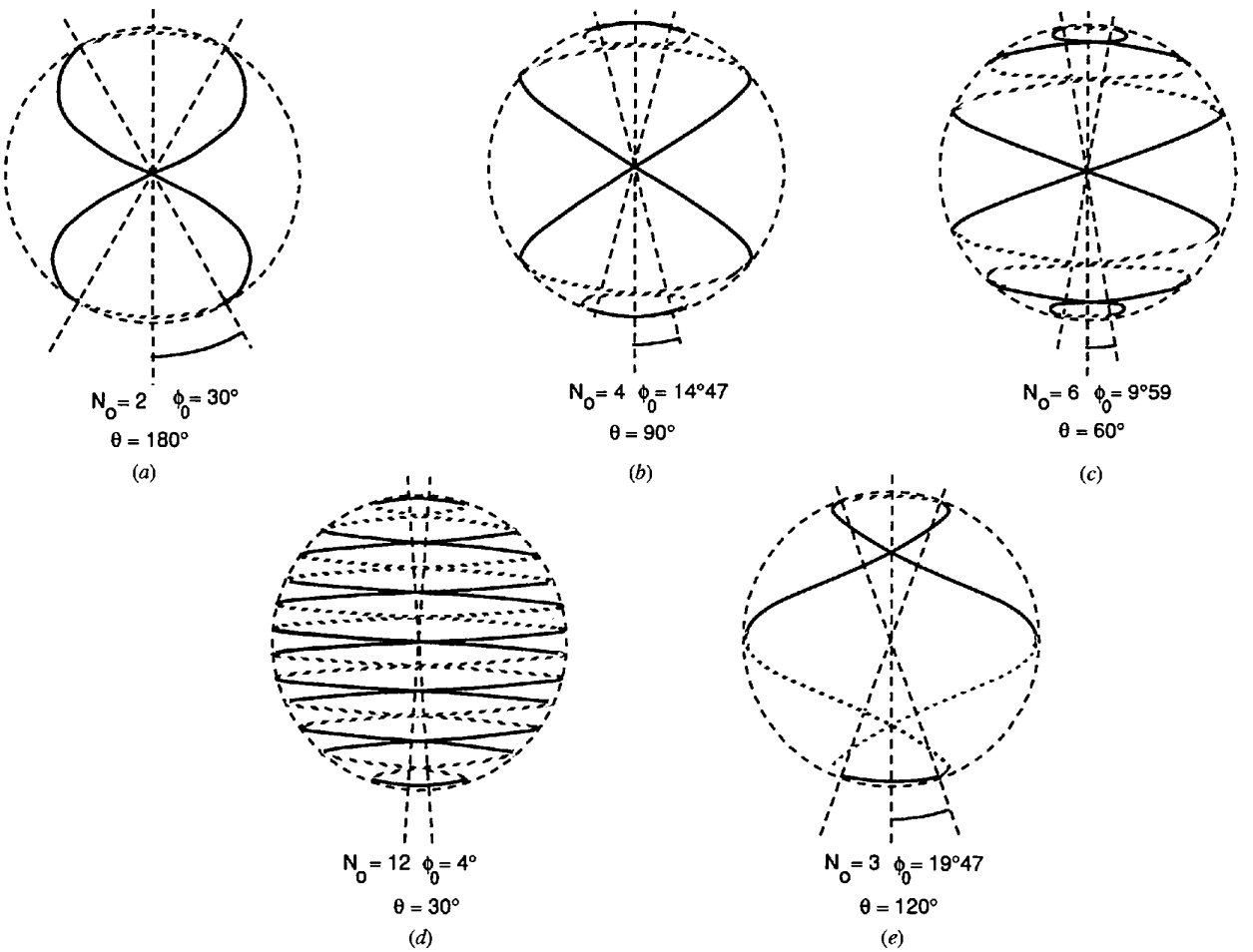

Fig. 19. Schematic view along a symmetry plane of the loci corresponding to various values of ϕ_0 leading to integer values of $1/\sin\phi_0 = N_0$. If N_0 is even (2, 4, 6, 12), the curve belongs to the point group $mm2$; if N_0 is odd, it belongs to the point group $2/m$.

If p and q are incommensurate, closed spirals are not formed and the spherical band between $\alpha = -(\pi/2 - \phi_0)$ and $\alpha = +(\pi/2 - \phi_0)$ is filled completely.

A complex multiturn spherical spiral is shown in a cylindrical representation (ψ, $\sin\alpha$) in Fig. 20, illustrating the particular case

$$1/\sin\phi_0 = p/q = 17/5 = 3 + (2/5) \quad (N = 3; \varepsilon = 2/5).$$

The actual pattern contains five sinusoids extending over a total interval in ψ of 34π [$5 \times 6\frac{4}{5}\pi$], corresponding to 17 turns of the spiral. To read this diagram, it should be realized that in order to shorten the length of the graph the spiral has been compressed along the ψ axis. In particular, the same numbers n and n' ($n = 1, 2, 3, 4, 5$) represent the same point and ensure furthermore that the curve continues with the correct phase. The compression is achieved by shifting the graph backwards (*i.e.* towards the origin) over $\Delta\psi = 6\pi$ after each period of the sinusoid ($2\pi/\sin\phi_0 = 6\frac{4}{5}\pi$).

The number of intersection points with the equator is clearly ten ($= 2q$), five intersections occur moving southwards and five moving northwards; the separation of successive intersection points is $\frac{4}{5}\pi$ ($= 2\pi\varepsilon$). The actual spatial shape is obtained by projecting the curves on the sphere as shown in Fig. 8.

6.4.8. *Intersection points with the equator, N_0 fractional.* If the electron beam is incident parallel to the fibre axis, the Ewald plane is the equator plane. The intersection points with this plane are given by $\alpha = 0$, *i.e.* by

$$\sin[(\sin\phi_0)\psi] = 0 \tag{29}$$

and alternatively by

$$\psi = k\pi/\sin\phi_0 = (p/q)/k\pi = (N + r/q)k\pi \tag{30}$$

(n, p, N, k integers).

If N is even, for instance $N = 2m$ (m = integer),

$$\psi = 2km\pi + k\pi(r/q) \pmod{2\pi}. \tag{31}$$

The spacing between zeros is thus $\pi(r/q)$, the origin of the sequence being $\psi = 0$ ($k = 0$). The number of zeros is $2\pi/\pi(r/q) = 2q/r$; if q/r is an integer, their number is finite.

If N = odd, for instance $N = 2m + 1$ (m = integer),

$$\psi = k(2m + 1)\pi + k\pi(r/q) \pmod{2\pi}. \tag{32}$$

$\psi = 0$ ($k = 0$) and $\psi = \pi$ ($k = 1$) are the origins of two sequences both with a repeat $2\pi(r/q)$. This leads to two interleaving sequences. If q/r is an integer, the two sequences form together a sequence with a spacing $\pi(r/q)$.

In actual fact, $\psi(p/q)k\pi$ will lead to a finite number of intersection points if p/q can be developed in a finite continued fraction such as $p/q = n_1 + 1/(n_2 + 1/n_3)$ where the n_j are integers.

6.4.9. *Single spiral spot pattern under normal incidence.* At normal incidence ($\gamma = 0$), the Ewald plane can be represented by $\psi = \psi_E + k\pi$ (k = integer). We assume $\sin\psi_0 = 1/N_0$ (N_0 = integer = number of turns). The number of intersection points is twice the number of turns: $2N_0$. The latitudes of these intersection points can be computed from

$$\sin\alpha_k = (1 - 1/N_0^2)^{1/2} \sin[(\psi_E + k\pi)/N_0] \tag{33}$$

with $k = 0, 1, \ldots, 2N_0 - 1$. Odd and even values of k lead to intersection points left and right, respectively, of the projected fibre axis. Symmetric patterns are obtained for two cases, $\psi_E = 0$ and $\psi_E = \pi/2$. For $\psi_E = 0$, one has

$$\sin\alpha_k = (1 - 1/N_0^2)^{1/2} \sin(k\pi/N_0). \tag{34}$$

The points with $k = 0$ and $k = N_0$ are situated on the equator, $\alpha = 0$. Extrema are reached for $k = N_0/2$ and $k = 3N_0/2$ (for N_0 even).

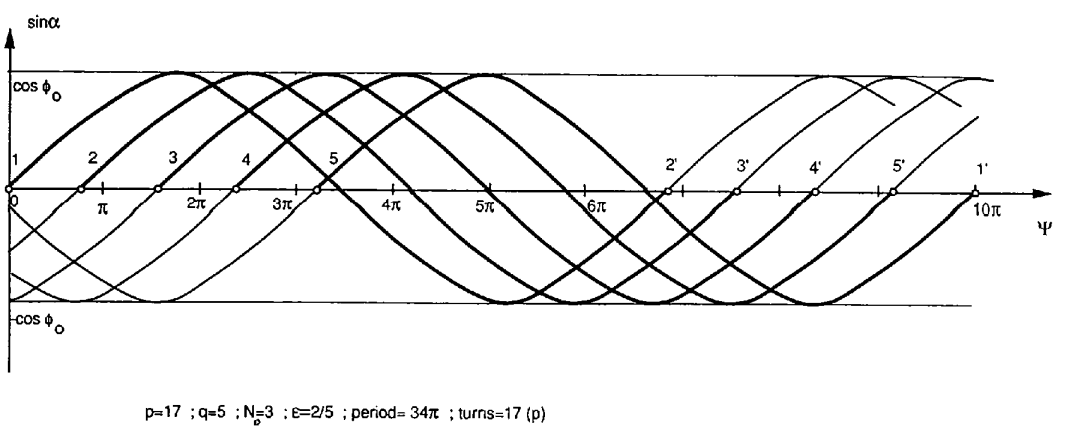

Fig. 20. 'Compressed' view of a complex multiturn spherical spiral with $1/\sin\phi_0 = 17/5$, represented in cylindrical projection ($\sin\alpha$ *versus* ψ). The five sinusoids represent in fact a single sinusoid obtained by connecting the points n' to n after each period. The total period of the spiral is 34π.

In the specific case $N_0 = 6$, the points corresponding to $k = (0, 6)$ lead to $\alpha = 0$, and the pairs of k values $(0, 6)$, $(2, 4)$, $(8, 10)$, $(5, 1)$ and $(11, 7)$ lead to double points, whereas $k = 3$ and $k = 9$ lead to single points (the extrema). The pattern has a line of symmetry perpendicular to the fibre axis (point group m) (Fig. 21*a*). In the case $N_0 = 3$, all spots are single and the symmetry is described by the planar point group $mm2$ (Fig. 21*c*).

For $\psi_E = \pi/2$, the spot positions are given by

$$\sin\alpha_k = (1 - 1/N_0^2)^{1/2} \sin[(2k + 1)\pi/2N_0]. \quad (35)$$

For $N_0 = 6$ (even), all points are single and the pattern belongs to the planar point group $mm2$ (Fig. 21*b*). For $N_0 = 3$ (odd), half of the points are double, the two remaining ones are single. The pattern belongs to the planar point group I (Fig. 21*d*).

The spot patterns for intermediate positions of the Ewald plane $0 < \psi_E < \pi/2$ result if the double spots are assumed to split into two spots situated asymmetrically, one on each side of the double-spot position. Simultaneously, the single spots move away from the closest double-spot position as indicated by arrows in Figs. 21(*a*), (*d*).

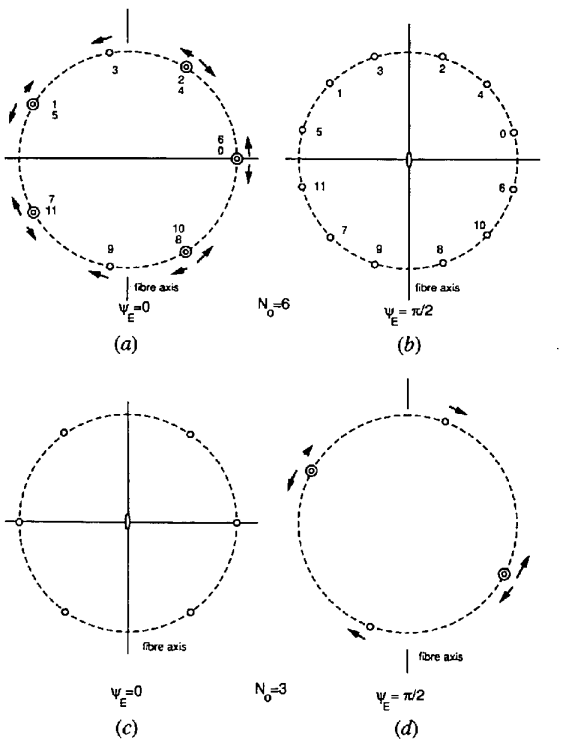

Fig. 21. Spot patterns produced by the intersection of a single spherical spiral with two different azimuthal positions of the Ewald plane under normal incidence ($\gamma = 0$). (*a*) $N_0 = 6$, $\psi_E = 0$; (*b*) $N_0 = 6$, $\psi_E = \pi/2$; (*c*) $N_0 = 3$, $\psi_E = 0$; (*d*) $N_0 = 3$; $\psi_E = \pi/2$. The arrows indicate how the spots move on tilting (*a*) and (*b*) from $\psi_E = 0$ to $\psi_E = \pi/2$ or (*d*) and (*e*) from $\psi_E = \pi/2$ to $\psi_E = 0$.

6.5. *Diffuse scattering*

6.5.1. *General considerations.* The discussion of diffuse-intensity streaks associated with conical fibres is an extension of the discussion for cylindrically symmetric fibres (Zhang *et al.*, 1993). In particular, the c^* directions are no longer confined to a plane normal to the fibre axis but are now situated on a double cone of revolution with its apex in the origin, with semi-apex angle $\pi/2 - \phi_0$ and with a rotation axis parallel to the fibre axis. Sharp $00l$ reflections are produced as intersections of the Ewald plane with circles with radii $r_l = lc^* \cos\phi$, situated on this double cone (Fig. 22), *i.e.* with $\alpha = \pi/2 - \phi_0$.

6.5.2. *Cylindrical case.* The diffuse intensity distribution in diffraction space is conveniently described by circular rings or coronae associated with the reflections other than $00l$ (Fig. 23). The presence of disorder in the stacking of the c layers, which is very often present, does not affect the $00l$ reflections but it causes hkl reflections to become streaked along $\mathbf{c}^*$. This streak is perpendicular to the vector $\mathbf{g}_{hk0}$ and situated in the $(hk0)^*$ plane. It is thus tangent to the circular locus. As a consequence of the rotation symmetry, the intensity distribution in the $(hk0)^*$ plane is represented by a ring-shaped area, sharply limited inwards by the circle with radius $\mathbf{g}_{hk0}$ and fading out in the outward direction. This ring or corona is also obtained by the rotation of a streak tangent to the circle. This leaves the inner circle of the ring sharp but the streak sweeps the outer part, which gradually fades out, owing to the increase in circumference of the outer circles (Fig. 23).

The construction of the diffuse intensity coronae in the cylindrical case illustrated in Fig. 24(*a*) can be formulated in a way that allows us to generalize it to the conical case (Amelinckx *et al.*, 1994, 1995; Liu & Cowley, 1994*a*,*b*; Baker, 1989; Tibbets, 1984):

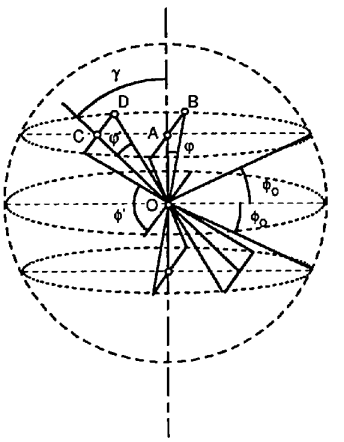

Fig. 22. Relationship between the true angle $\varphi = 90° - \phi_0$ between $00l$ rows under normal incidence ($\gamma = 0$) and the angle $\varphi' = 90° - \phi'$ measured on the diffraction pattern: $\sin\phi_0 = \sin\phi' \cos\gamma$.

(*a*) consider the sphere of all *hk*0 reflections, *i.e.* with radius $\mathbf{g}_{hk0}$ and with its centre at the origin of diffraction space (Fig. 24*b*);

(*b*) consider the locus of a particular *hk*0 reflection; this is a small circle (*C*) on this sphere situated in a plane normal to the fibre axis;

(*c*) consider the cylinder based on this circle (*C*) with generators parallel to the fibre axis;

(*d*) consider a point *A* on (*C*);

(*e*) draw the tangent plane Π to this cylinder, in *A*;

(*f*) the locus of all c^* streaks is a plane Σ normal to the fibre axis;

(*g*) consider the intersection (*l*) of the tangent plane Π and the plane Σ brought through *A*. This produces the streak *l* in *A*; it is tangent to (*C*);

(*h*) repeat this operation in all points of the locus (*C*);

(*i*) the result is the ring-shaped corona of diffuse intensity mentioned above;

(*j*) intersecting these coronae with the Ewald plane produces the streaks in the diffraction pattern and in particular shows why they are sharply limited at the diffraction spot and fade out outwards and why they are parallel to the row of sharp 00*l* reflections.

6.5.3. *Conical case.* We now generalize this procedure to the case of conical fibres (Fig. 24*c*) by considering which changes have to be made to the different steps:

(*a*) remains unchanged;

(*b*) the locus of a particular reflection of this kind is a spherical spiral (*S*) on the sphere, as discussed above;

(*c*) consider the cylindrical surface based on (*S*) with generators parallel to the fibre axis;

(*d*) consider a point *A* on (*S*);

(*e*) draw the tangent plane Π to the cylinder in *A*;

(*f*) the locus of all c^* directions is a double cone with semi-apex angle $\pi/2 - \phi_0$ and with a rotation axis parallel to the fibre axis;

(*g*) consider the two intersections of the tangent plane Π in *A* with the double cone Σ, the latter being shifted so as to bring the apex in *A*. These intersections l_1 and l_2 are *two* streaks associated with the point *A*; they are parallel to the directions of the linear arrays of sharp 00*l* spots;

(*h*) repeat the operation in all points of the locus (*S*);

(*i*) the result is a complex surface, represented schematically in Fig. 24(*a*).

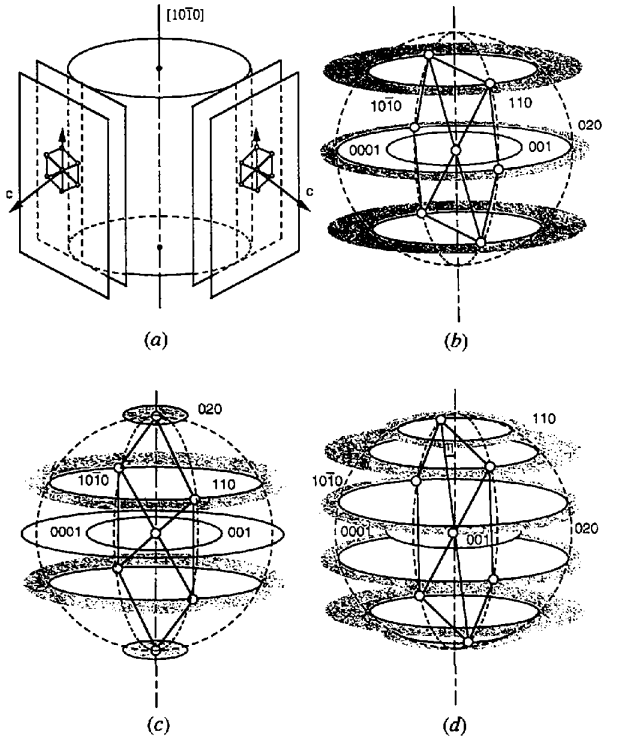

Fig. 23. Diffraction space due to cylindrically wrapped layers; diffuse scattering. (*a*) The layer planes are tangent everywhere to a cylinder. Two orientations of the layer planes $(00.1)_h$ or $(00\bar{2})_o$ are shown. (*b*), (*c*), (*d*) The loci of the first-order reflections {10$\bar{1}$0} [or $(110)_o$ and $(010)_o$] are shown. They are circles sharply limited inwards but fading outwards. The loci of the $(00.2)_h$ [$(00\bar{2})_o$] reflections are sharp circles. (*b*) Fibre axis is parallel to $[11\bar{2}0]_h$ ($[010]_o$). (*c*) Fibre axis is parallel to $[10\bar{1}0]_h$ ($[100]_o$). (*d*) Chiral fibres; the chiral angle is η.

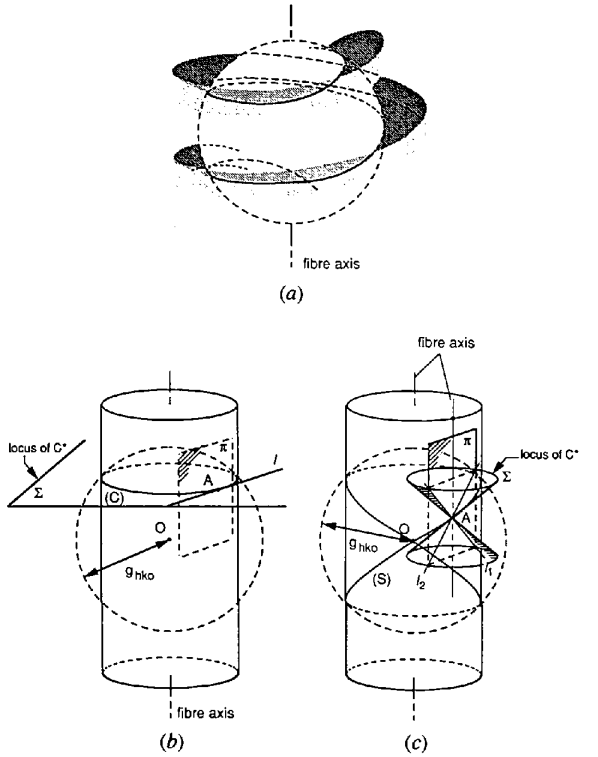

Fig. 24. (*a*) Locus in diffraction space described by a reciprocal-lattice node (except 00*l* nodes). The locus is spherical spiral limiting inwards a *V*-shaped diffuse belt, leading to diffuse streaks. This surface is a generalization of the diffuse coronae represented in Fig. 23. (*b*) Construction of diffuse coronae in the cylindrical case. (*c*) Construction of the diffuse surface in the conical case.

(*j*) the intersections of this surface with Ewald's plane produce the *V*-shaped streak configurations associated with all spots except for 00*l*. The streaks are parallel to the rows of sharp 00*l* spots; they form a *V*-shaped arrangement, the point of the *V* coinciding with an intersection point of the conical spiral with the Ewald plane (Fig. 9*e*).

In order to help visualize the diffuse intensity surface, we consider the hypothetical case where the curve (*S*) remains a circle but a pair of intersecting lines l_1 and l_2 is nevertheless present in a point of (*S*). A surface is now generated in the way described above by rotating the set of two intersecting lines l_1 and l_2, which are assumed to be symmetrically inclined with respect to the rotation axis. The resulting surface of revolution is a hyperboloid of one sheet, which is clearly a ruled surface. The actual surface of interest can now be approximated by cutting this hyperboloid and deforming its guiding circle into a spherical spiral (*S*). Note that as $\phi_0 \rightarrow 0$ the actual surface, as well as its approximation, reduces to the diffuse corona normal to the fibre axis, considered in the cylindrical case.

Locally, it is a good approximation to consider the *V* surface as part of a hyperboloid of one sheet with the double cone of c^* directions as the asymptotic cone. It then becomes clear why certain streaks look like branches of a hyperbola; if the surface is intersected by a plane (the Ewald plane!) that is not tangent to the surface, the intersection curve is a hyperbola with the two c^* directions as asymptotes. If the intersecting plane is tangent to this ruled surface, it intersects along two straight lines forming an angle $2\phi'$ as for instance in Fig. 25.

6.6. *Superperiods*

As already mentioned above, successive sheets are rotated by θ about the local normal to the cone surface. If θ is an integer fraction of 360°, the same orientation will repeat after $N = 360/\theta$ turns provided the sheet has no rotational symmetry. A microstructure with a period Nc will result, producing the superperiod along [001] (Figs. 5, 10 and 27). The microstructure rotates as a whole by θ on considering points on a closed path along the periphery of the cone, *i.e.* surrounding the cone axis, but it remains parallel to itself in points along a straight path through the apex. Since high-resolution images reveal the (001) planes where they are tangential to the incident electron beam, *i.e.* along lines through the apex, the superperiod of this microstructure is visible in such images.

If $360/\theta$ is p/q, where p and q are mutually prime, the sequence repeats only after p turns but it is modulated with a period qc. If θ is incommensurate with 360°, the microstructure is not periodic and quasi-continuous streaks along the two c^* directions will be formed. These simple relations are only valid if the cone is formed from a single bilayered lamella. If the conical sheet has a thickness τc and has rotation symmetry with multiplicity m about the local [001] directions, the superperiod will be $N_s c$ with

$$N_s = (360/\theta)(\tau/m). \tag{36}$$

It has long been suspected that cylindrical fibres may form scrolls with scroll steps of one or more bilayers (Jagodinski & Kunz, 1954*a*). The observations of Yada (1971) demonstrated that cylindrical fibres with scrolls of up to at least four layers are common in some natural samples. It is therefore reasonable to assume that multiple sheets also occur in conically wound fibres, as is suggested by their morphology with thick growth steps (Figs. 15 and 26). In these cases, the superperiod may become larger than that corresponding to the cone angle. It should be noted that, for a detailed interpretation, the true cone angle ϕ_0 has to be known; in inclined specimens, the observed angle ϕ' is larger than the true cone angle ϕ_0 as shown by (15). Unfortunately, the inclination angle γ is usually unknown and cannot be deduced easily from geometrical features of the diffraction pattern without assuming a value for ϕ_0. We will show how, nevertheless, a number of observations can be interpreted.

In Fig. 5, the streaks parallel to $\mathbf{c}^*$ clearly show main reinforcements corresponding to a period $4c$ and much weaker spots roughly midway between the main spots.

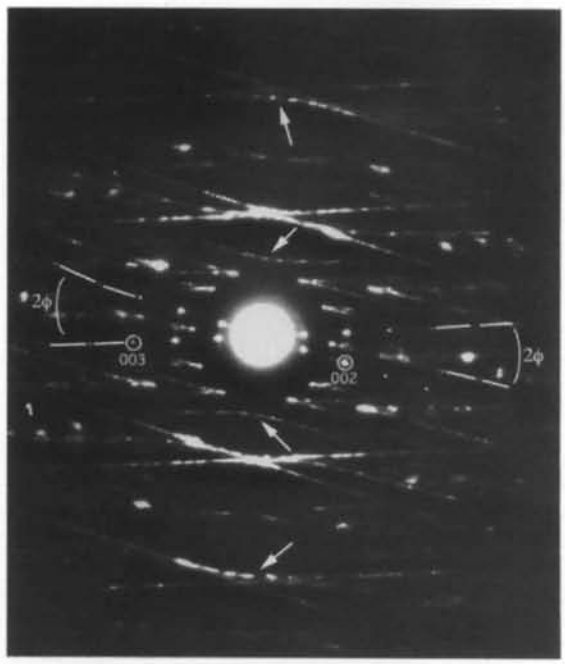

Fig. 25. Diffraction pattern of synthetic conically wound chrysotile fibre. Outward oriented *V*-shaped streaks are attached to all diffraction spots (except for the sharp 00*l* spots). The cone angle is $2\phi_0 \simeq 19$–$20°$. Note the presence of hyperbola-shaped streaks as indicated by arrows.

The two c^* rows enclose an angle of about 20°, *i.e.* $\phi_0 \simeq 10°$, which is within the experimental error compatible with $\phi_0 = 9.58°$ or $\theta = 60°$ and $N_0 = 6$. The pattern of intense reflections is consistent with the intersection patterns of spirals with $N_0 = 6$, leading to 12 intersection points for each of the lower-frequency circles. The azimuth ψ_E must be closer to $\psi_E = 0$ than to $\psi_E = \pi/2$ (Fig. 21). The beam incidence is thereby assumed to be close to normal ($\cos\gamma \simeq 1$). From (36), a fourfold period can be obtained when $\tau = 2$ and $m = 3$. This is equivalent to assuming that the conical sheet consists of two bilayers and that the resulting stacking has threefold symmetry. This is the case for instance for the $2T$ polytype. However, it is worth noting that, strictly speaking, this stacking cannot be maintained as a consequence of the wrapping of the sheet and translation faults will occur. This does not affect the period since this is due to orientational variants. The weak spots also form an equidistant sequence with a period $\frac{1}{4}c^*$ but which is shifted with respect to the sequence of stronger spots over roughly $\frac{1}{8}c^*$. The reason is that the two sequences originate from two different nearby basic spots and are superimposed by chance owing to the particular specimen orientation with respect to the Ewald plane. Fig. 27 shows in the inset the high-resolution image of a fourfold period.

Also, the high-resolution image of Fig. 27 can consistently be interpreted on the basis of our model. The angle between the two sets of 001 fringes is 22°, *i.e.* $\phi_0 = 11°$. The closest (but smaller) special value is again 9.59°, suggesting that the specimen was tilted over an angle $\gamma = 45°$ [from (15)]. The observed sixfold period is obtained if $\tau = 2$ and $m = 2$, which means that the sheet is considered to be a two bilayer orthorhombic polytype.

Note that the growth layers observed on the surface have a thickness equal to twice the six-layer period. This 12-fold growth period is consistent with a crystallographic period of $6c$.

In Fig. 10, the angle between the two $00l$ rows is again $2\phi' \simeq 20°$ and thus compatible with $N_0 = 6$. This is also consistent with the presence of six spots on the low-frequency circles. Their configuration is a some-

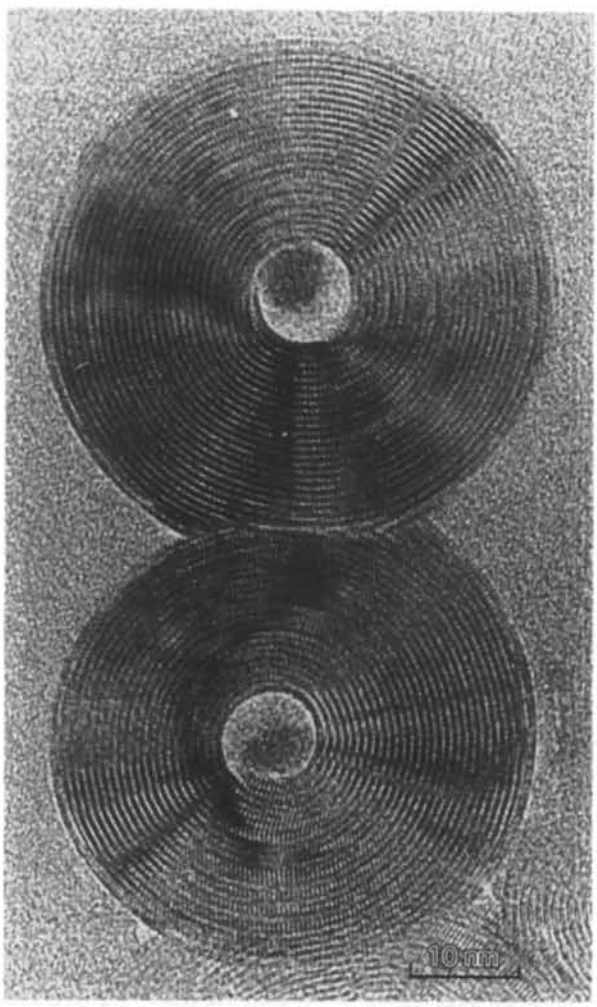

Fig. 26. High-resolution images along the fibre axis of a single-layer and of a double-layer cylindrical chrysotile scroll.

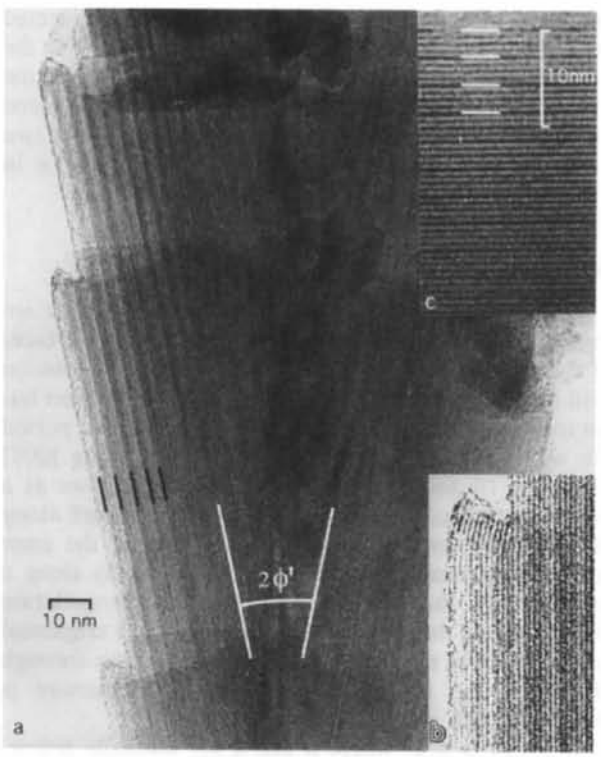

Fig. 27. (*a*) Lattice image of a synthetic conical chrysotile fibre. Note the sixfold superperiod along **c**, which is consistent with the apex angle of $2\phi_0 \simeq 20°$. (*b*) Magnified part of (*a*) exhibiting a sixfold superperiod. (*c*) Lattice fringes in chrysotile exhibiting a period of $4c$. The period is best observed under grazing incidence parallel to the fringes.

what tilted version of the configuration represented in Fig. 21(*a*) ($\psi_E = 0$, $N_0 = 6$). The superperiod deduced from the fine structure of the streaks is 6*c*; it can be generated in several ways for which $\tau = m$ [in (33)], *i.e.* $N_s = N_0$. Since m is limited to 1, 2, 3, 6, this is also the case for t. Note the strong preference for $N_0 = 6$.

6.7. *Sets of spherical spirals*

6.7.1. *Cylindrical projection; extended scheme representation.* As motioned in §5.1, a convenient way to represent the spatial spherical spiral in a plane is to make use of a Mercator-type cylindrical projection in which a point on the sphere P_s is projected on a point P_c on a cylinder that touches the sphere along the equator (Fig. 8). Since the azimuth in general exceeds 360°, the cylinder is assumed to be a scroll. The curve is periodic in many cases of interest; it is therefore sufficient to represent one period $\Delta\psi_T = 2\pi/\sin\phi_0$, which is in general a multiple of 2π. The scroll is unrolled to obtain the planar representation. Along the vertical direction, we plot $y = R\sin\alpha$, where R is the radius of the sphere ($R = |\bar{\mathbf{g}}_{10\bar{1}0}|$), and, along the horizontal direction, we plot $x = R\psi$. The resulting curve is a sinusoid with its origin at ψ_0 oscillating between $+\cos\phi_0$ and $-\cos\phi_0$, the extrema corresponding to $\psi = \psi_0 + \pi/(2\sin\phi_0)$ and $\psi = \psi_0 - [\pi/(2\sin\phi)]$. In Fig. 28, we have chosen $\psi_0 = 0$ for the sinusoid shown with the thicker line, and which will be considered separately. This planar curve allows one to visualize the properties of the spatial curve. It is clear that the intersection point with the equator must be a centre of symmetry on the spherical surface, *i.e.* $\alpha_n(\psi) = -\alpha_n(-\psi)$, as is also evident from (12).

The lines ψ = constant through the extrema are lines of symmetry, *i.e.*

$$\alpha_n[\pm(\pi/2\sin\phi_0) + \psi] = \alpha_n[\pm(\pi/2\sin\phi_0) - \psi]. \quad (37)$$

This property can also be verified directly with (12). The intersection points of the curve with itself, *i.e.* the double points, can be found by looking for symmetrically situated points (with respect to an extremum) for which the difference in azimuth is an integer number of 2π. Intersection points occur at the same azimuth, *i.e.* in the same radial planes as the extrema. Points are indicated by the same numbers as in Fig. 28, to the left.

The same type of graph allows us to represent in a simple manner the six spirals generated by the six node points of the first hexagon (the $10\bar{1}0$-type reflections) for which $\Delta x = \pi/3$ (Fig. 28). The similar sinusoids are shifted along the ψ axis over equal intervals $\Delta\psi = \pi/(3\sin\phi_0)$. This follows directly from (12) by noting that $\sin\alpha$ can be rewritten

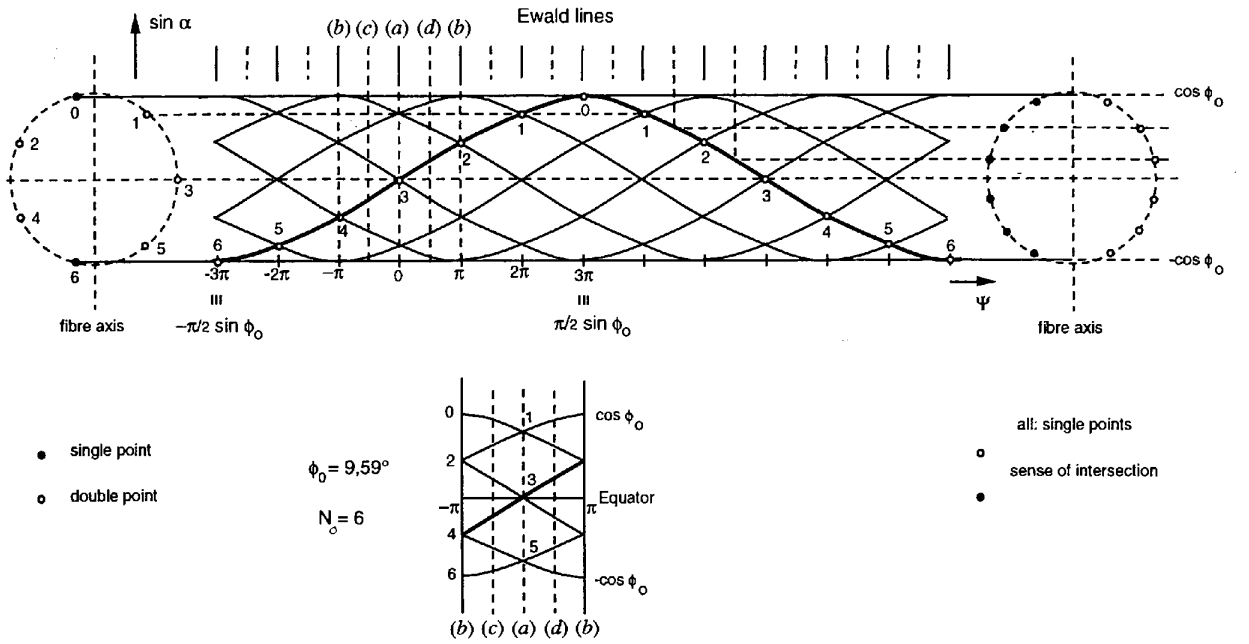

Fig. 28. (Top) Extended cylindrical projection ($\sin\alpha$ *versus* ψ) of the six identical closed spherical spirals corresponding to the six nodes of the first hexagon. The cone angle is $2\psi_0 = 19°$. The six sinusoids are phase shifted by 2π in the azimuth ψ. The period of each sinusoid is 12π in ψ ($2\pi/\sin\phi_0 = 12\pi$). The periodic vertical segments represent cylindrical projections of a single Ewald plane for the case $\gamma = 0$ (normal incidence). The full segments represent the Ewald plane through the double points; the dotted segments refer to the perpendicular plane ($\Delta\psi = 90°$). The corresponding diffraction spots of the first hexagon are represented left and right, respectively. (Bottom) Reduced scheme; the Ewald planes (*a*), (*b*) lead to the left spot pattern; (*c*), (*d*) to the right pattern. The 'sense of intersection' ('northwards' or 'southwards') has only a relative meaning.

$$\sin\alpha = \cos\phi_0 \sin[\psi \sin\phi_0 + \pi/3]$$
$$= \cos\phi_0 \sin[(\psi + \pi/3 \sin\phi)\sin\phi_0]. \quad (38)$$

For $\phi_0 = 9.58°$, $\Delta\psi = 2\pi$ and, for $\phi_0 = 4.78°$, $\Delta\psi = 4\pi$, whereas the periods are respectively 12π and 24π.

For the loci corresponding to the nodes of the second hexagon (*i.e.* for reflections of the type $11\bar{2}0$), a similar construction is possible: the radius of the sphere is different (it is now $R = |\bar{\mathbf{g}}_{11\bar{2}0}|$). Since the horizontal and vertical directions of the graph of Fig. 28 are scaled by the same factor R, the same curves can be used. However, since the two 'hexagons' of spots differ in orientation by 30°, the χ value in (13) has to be replaced by $\chi + 30°$). This would be reflected in the set of curves by a relative shift $\Delta\psi = \pi/(6 \sin\phi_0)$.

The construction that leads to the spot positions, *i.e.* the intersection of the spatial curve by the Ewald plane, in the case of normal incidence, is now represented as the intersection by a periodic set of lines (Ewald lines!) parallel to the vertical axis, the period being π.

When the Ewald plane is parallel to the fibre axis and passes through a maximum, it passes also through such double points. Such a section is shown in Fig. 28 where the periodic arrangement of full-line segments represents in fact a single Ewald plane, which intersects the cylindrical scroll after each half turn, *i.e.* along lines with a difference in azimuth $\Delta\psi = k\pi$ (k = integer). The arrangement of intersection points of the considered sinusoid with this particular plane ($\psi = 0$) is shown in the left circle: five points are double points; two points are single points: 12 points in total. When the Ewald plane is still parallel to the fibre axis but is now perpendicular to the previous one, *i.e.* its azimuth is now $\psi = k\pi + \pi/2$, this is represented by the dotted segments in Fig. 28. All 12 intersection points with the considered sinusoid are now single and the section is represented on the right of Fig. 28. This illustrates that the diffraction pattern is very sensitive to the azimuth, *i.e.* to the orientation of the fibre along its long axis and not only to the direction of the incident beam. Two extreme cases were shown here. The left one has only a horizontal line of symmetry whereas the right one has *mm*2 planar symmetry.

For intermediate azimuthal orientations of the Ewald plane, the pattern will lose the specific symmetries exhibited here. Moreover, if the beam incidence is not normal, additional deformation of the pattern will occur.

6.7.2. *High-symmetry cases.*

6.7.2.1. *Spot positions of the first hexagon (reflections of the type 1010).* From the geometrical construction in Fig. 28, we concluded that, in the specific case shown there ($N_0 = 6$), the set of intersection points with the Ewald plane for normal incidence ($\gamma = 0$) is the same whether a single spiral or a set of six spirals corresponding to the six reciprocal-lattice nodes was considered. This greatly simplifies diffraction space and hence leads to simple diffraction patterns. Unfortunately, this simplicity is not a general property of the sets of spirals. We shall show that it is only true for $N_0 = 6$ and if $\gamma = 0$ such that $\alpha_{k,n} = \chi_{E,k,n}$.

The property follows from purely geometrical considerations based on the generation process of the spirals. The angular difference in χ_E between two adjacent nodes j and $j+1$ (mod 6) in the plane Π of Fig. 7(*a*) is $\pi/3$. One node is thus transformed into the second one by a rotation over $\pi/3$ about the a_2 axis. Such a rotation is also produced if one follows one node (*i.e.* the same spiral) after a rotation of the plane Π over 2π about the a_1 axis (Fig. 7*a*). The rotation over 2π about the a_1 axis coupled with the rotation about the a_2 axis is thus a symmetry operation for the spiral. We conclude that the six node points are always situated on the same spiral, as illustrated in Fig. 18 by the hexagon of points.

Analytically, this follows from (13). The latitudes $\alpha_{k,n} = \chi_{E,k,n}$ (for $\gamma = 0$) are given by

$$\sin\alpha_{k,n} = \cos\phi_0 \sin[(\psi + k\pi)/6 + n\pi/3], \quad (39)$$

where $\cos\phi_0 = 0.986$ for $N_0 = 6$; k = integer, $n = 0, 1, \ldots, 5$. This can be rewritten as

$$\sin\alpha_{k,n} = 0.986 \sin\{[(\psi + 2n\pi) + k\pi]/6\}. \quad (40)$$

The sequence of $\alpha_{k,n}$ values generated for $n \neq 0$ is thus the same as that for $n = 0$ for any value of the ψ, *i.e.* the two spirals are identical since adding $2n\pi$ to ψ does not change the sequence. All six spirals generated by the six nodes thus coincide but the k values belonging to the given point of the locus corresponding to the node n differ by $2n$ from the k value of the same point considered as belonging to the locus $n = 0$.

Simplifications also arise in the cases $N_0 = 3$ and $N_0 = 2$. For $N_0 = 3$, the six node points generate two different loci. The node points with n even generate one locus and the ones with n odd the other locus. This follows from similar geometrical considerations as given above, but it can be shown analytically. One has

$$\sin\alpha_{k,n} = 0.942 \sin[(\psi + k\pi)/3 + n\pi/3]. \quad (41)$$

If $n = 2m$ (m = integer), this can be rewritten as

$$\sin\alpha_{k,n} = 0.942 \sin\{[(\psi + 2m\pi) + k\pi]/3\}, \quad (42)$$

which shows that the sequence of points is the same as that for $n = 0$. If $n = 2m + 1$, one can write

$$\sin\alpha_{k,n} = 0.942 \sin\big(\{[\psi + (2m+1)\pi] + k\pi\}/3\big). \quad (43)$$

This represents the same sequence as for $n = 0$ but rotated over π. The nodes $n = j$, $j+2$ and $j+4$ ($j = 0, 1$) thus generate the same spiral.

Finally, for $N_0 = 2$, the six node points generate three different loci. One has

$$\sin\alpha_{k,n} = 0.866\sin[(\psi + k\pi)/2 + n\pi/3]. \quad (44)$$

For $n = 3m$, this can be rewritten as

$$\sin\alpha_{k,n} = 0.866\sin\{[(\psi + 2m\pi) + k\pi]/2\} \quad (45)$$

The curve generated by the node $n = 3$ is then the same as that generated by the node $n = 0$. For $n = 3m \pm 1$, one obtains

$$\sin\alpha_{k,n} = 0.866\sin\{[\psi + (2m \pm \tfrac{2}{3})\pi + k\pi]/2\}, \quad (46)$$

which shows that the loci generated by $n = j$ and $n = j + 3$ are the same and moreover successive nodes generate curves differing by $2/3\pi$ in orientation. There are thus three different curves generated by the six nodes.

If N_0 is a multiple of six, reciprocal space is still a single spiral (see *e.g.* $N_0 = 12$ in Fig. 19*d*) for all six nodes of a hexagon. As a result of the coupled rotations $\Delta\chi = (1/12)\Delta\psi$, it is clear that ψ has to increase by $\Delta\psi = 4\pi$ to cause a change $\Delta\chi = \pi/3$. This coupled rotation corresponding to $\Delta\psi = 4\pi$ is thus a symmetry operation for the spiral. This means that successive reciprocal-lattice nodes of the same hexagon along the spiral are separated by two full turns, whereas this was a single turn in the case $N_0 = 6$. This can be concluded from (13) by noting that

$$\sin[(\psi - \psi_0)/12 + n\pi/3] \equiv \sin\{[(\psi + 4\pi n) - \psi_0]/12\}. \quad (47)$$

The latitude of the node 0 for azimuth ψ is the same as that of node n for $\psi = 4\pi n$.

Conversely, one might ask the question under what conditions the six spirals coincide, either all or only a fraction of them.

From (13), we find in the high-symmetry cases $(1/\sin\phi_0 = N_0)$ $(N_0 = \text{integer})$

$$\sin\alpha = (1 - 1/N_0^2)^{1/2}\sin[(\psi - \psi_0)/N_0 + n\pi/3]. \quad (48)$$

This expression must now be independent of the considered node, *i.e.* of n. This will be the case if

$$[(\psi - \psi_0)/N_0] + (n\pi/3) = (\psi - \psi_0)/N_0 \,(\text{mod}\, 2\pi) \quad (49)$$

or if

$$nN_0(\pi/3) = 2k\pi \quad (k = \text{integer}) \quad (50)$$

or if $nN_0 = 6k$. The product nN_0 will only be a multiple of 6 for all integer values of n $(0, 1, \ldots, 5)$ if $N_0 = 6$. In this case, the six reciprocal-lattice nodes thus generate only a single spiral.

If $N_0 = 3$, not all n values lead to a sixfold symmetry; only even n values are now satisfied and hence only half of the nodes, for instance $n = j$, $j + 2$ and $j + 4$ $(j = 1, 2)$ are on the same spiral.

If $N_0 = 2$, only n values that are a multiple of 3 lead to multiples of 6 for $6k$. This means that now only one third of the nodes (*i.e.* two nodes) are on the same spiral. For instance, $n = j$ and $j + 3$ $(j = 1, 2, 3)$. Since 6 has no other factors than 6, 3 and 2, there are no other solutions.

Table 2. *Point groups of single spherical spirals and of a set of spherical spirals*

	Single spiral	Complete set
$N_0 = 2$	*mm*2	$\bar{3}2/m$
$N_0 = 3$	$2/m$	$2/m\ 2/m\ 2/m$
$N_0 = 6$	*mm*2	*mm*2

The planar point group of the diffraction pattern can obviously be obtained as the section by the Ewald plane of the spatial point group of the set of loci.

How are the spirals related when more than one is present?

For $N_0 = 3$, the condition $nN_0(\pi/3) = 2k\pi$ $(k = \text{integer})$ will be satisfied for n even $(= 2k)$. However, for n odd $(= 2k + 1)$, one finds $nN_0(\pi/3) = (2k + 1)\pi$. This means that the spiral corresponding to odd values of n differs in azimuth by π from the spiral corresponding to even values of n. The two spirals are thus related by a binary symmetry axis parallel to the fibre axis.

For $N_0 = 2$, the difference in azimuth $nN_0(\pi/3)$ will be $2k\pi$ only if $n = 3k$. If $n = 3k + 1$, this expression becomes $nN_0(\pi/3) = 2k\pi + (2\pi/3)$ and for $n = 3k - 1$ it becomes $2k\pi - (2\pi/3)$. This clearly means that the three spirals, each corresponding to those reciprocal node points, differ by 120° in azimuth. The three spirals are thus related by a ternary symmetry axis parallel to the fibre axis.

For the high-symmetry cases $(N_0 = 2, 3, 6)$, the spatial point group of the diffraction space, generated by the *hk*0 nodes, can now be given (see Table 2).

6.7.2.2. *Spot positions of the second hexagon (i.e. reflections of the type 1120).* The set of loci generated by the second hexagon of *hk*0 nodes is situated on the sphere with radius $g_{11\bar{2}0} = 3^{1/2}\, g_{10\bar{1}0}$. Within plane Π, the configuration of the second hexagon nodes is rotated (Fig. 7*a*) over 30° in χ about a_2. According to (9), one has $\Delta\chi = \sin\phi_0\,\Delta\psi$. For $N_0 = 6$, the change in azimuth of the set of loci is $\Delta\psi = (1/\sin\phi_0)\Delta\chi = 6(\pi/6) = \pi$. One concludes that the set of loci produced by the second hexagon is related to the set of loci produced by the first hexagon by a similarity operation with a scale factor $g_{11\bar{2}0}/g_{10\bar{1}0} = 3^{1/2}$ followed by a rotation of π about the fibre axis. Analogous conclusions hold for different N_0 values; for $N_0 = 3$, the difference in azimuth is $3(\pi/6) = \pi/2$ and, for $N_0 = 2$, this is $2(\pi/6) = \pi/3$.

In the cylindrical case and for $\gamma = 0$, the α values of the spots owing to the second hexagon differ by 30° from those of the first hexagon and this is independent of the orientation of the fibre about its axis.

In the conical case, this is no longer true. The $\alpha_{n,k} = \chi_{n,k}$ spot positions for the second hexagon in the case $N_0 = 6$ for $\psi_E = 0$ and $\psi_E = \pi/2$ ($\gamma = 0$) are shown in Fig. 29. These angular positions are derived from the relations

$$\text{for } \begin{cases} \psi_E = 0 \\ n = 0 \end{cases} \qquad \sin\alpha_{k,0} = 0.986 \sin[(k+1)\pi/6] \tag{51}$$

$$\text{for } \begin{cases} \psi_E = \pi/2 \\ n = 0 \end{cases} \qquad \sin\alpha_{k,0} = 0.986 \sin[(2k+3)\pi/12]. \tag{52}$$

The k values of the different positions are indicated in Fig. 29.

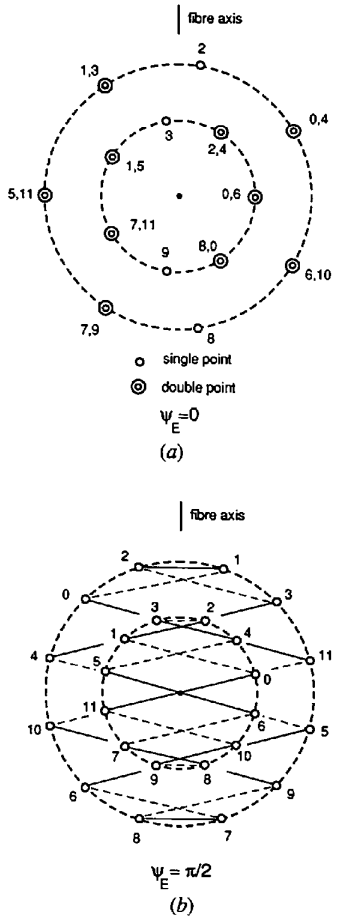

Fig. 29. Schematic representation of the computed spot positions for the high-symmetry situations. (*a*) $N_0 = 6$, $\psi_E = 0$. The positions are shown for the first and second hexagon of nodes. The six nodes produce a single spherical spiral. Single and double points are present. (*b*) $N_0 = 6$, $\psi_E = \pi/2$. The spot positions of the first and second hexagons are radially aligned. The full and dotted lines suggest the spirals that produce the spot positions. All positions are single.

The difference in orientation by π of the two shells of positions is evident from Fig. 29(*a*) ($\psi_E = 0$). The resulting configuration is essentially different from that in the cylindrical case. The configuration is even more strikingly different in the case $\psi_E = \pi/2$. The angular positions of the spots are now the same for the two shells even though the azimuthal orientation of the two spirals differs by π.This orientation difference becomes evident when connecting the positions by lines suggesting a schematic representation of the spirals of which they are the intersection points. This was done in Fig. 29(*b*) for the two shells.

In the high-symmetry case $N_0 = 6$ considered here, the six nodes of a shell generate a single spiral, as shown above. Figs. 29(*a*) and (*b*) can thus be compared with diffraction patterns made under the appropriate conditions, *i.e.* for $\gamma = 0$, $\psi_E = 0$ or $\psi_E = \pi/2$.

The cases $N_0 = 3$ and $N_0 = 2$ can be discussed similarly.

The large number of independent parameters, ϕ_0, γ, ψ_E, determining the diffraction pattern make a systematic study of the diffraction effects tedious. Observations made under the exact symmetry conditions described above have not been made systematically so far but the available diffraction patterns can consistently be interpreted in terms of the described model.

In Fig. 10, the first and second 'hexagons' of spots (*i.e.* spots $hk0$ with $h + k = 2$ and $h + k = 4$) differ by roughly 30° in agreement with Fig. 29(*a*); we conclude that the condition $\psi_E \simeq 0$ was approximately satisfied. In Fig. 25, on the other hand, the spots in the first and second hexagons are roughly radially aligned, suggesting that ψ_E is close to $\pi/2$.

The orientation relation between the first and second hexagons of spots is important because it provides a means to determine the azimuth of the Ewald plane from information present in the diffraction pattern.

6.7.3. *Intersection points; spot positions; general case.* The algorithm determining the intersection points of the loci with the Ewald sphere (plane!) and hence the positions of the diffraction spots in that plane is as follows. The equations of the loci (13) are of the form $F_1(\psi, \alpha; \phi_0, n) = 0$, where ϕ_0 is a parameter determined by the cone angle of the fibre and n an integer corresponding to the considered reciprocal-lattice node. The equation for the Ewald plane [(4), (5)] is of the form $F_2(\psi, \alpha; \psi_{0,E}\gamma) = 0$, where γ is a parameter determined by the inclination of the Ewald plane (Fig. 14). The solution of the set of non-linear equations $F_1 = 0$, $F_2 = 0$ leads to pairs $(\psi_{n,k}, \alpha_{n,k})$ for a given set of parameters ϕ_0, $\psi_{0,E}$ and γ. The index k refers to the different intersection points of the same spherical spiral with a given n value. The number of k values depends on the number of turns of the spherical spiral, which is essentially determined by ϕ_0 (see

Table 1). What we need for a comparison with the observations are the angular positions in the Ewald plane $\mu_{n,k}$ corresponding to the $\alpha_{n,k}$; they are given by $\mu_{n,k} = \arcsin(\sin\alpha_{n,k}/\cos\gamma)$ [from (6)]. For normal incidence ($\gamma = 0$), $\mu_{n,k} = \alpha_{n,k}$.

Instead of solving the system of equations $F_1 = 0$, $F_2 = 0$, numerically one obtains a better insight into the geometry of the diffraction spots by solving the system graphically. One plots $F_1(\alpha_1\psi_1; \phi_0, n)$ for different values of ϕ_0 and for $n = 0, 1, \ldots, 6$. If the unrolled cylindrical reference system as described above is used, $\sin\alpha$ *versus* ψ is plotted and the spherical spirals are represented as sinusoids, the curves corresponding to different n values are shifted over $\pi/(3\sin\phi_0)$. This graph (Fig. 28) allows us to discuss the symmetry of the pattern for certain special orientations of the Ewald plane. We consider first the same orientations as for a single sinusoid $\gamma = 0$, *i.e.* normal incidence and azimuths $\psi = 0$ and $\psi = \pi/2$. For these cases, the Ewald planes in the graph are lines parallel to the vertical axis. Owing to the scroll nature of the projection cylinder, a single Ewald plane is imaged by a periodic sequence of parallel lines. The full 'Ewald lines' in Fig. 28, top, represent the Ewald plane through the double points of the spherical spiral, whereas the dotted lines represent the Ewald plane perpendicular to the latter. The resulting configuration of intersection points, which determines the position of the diffraction spots, are shown left and right in the upper part of Fig. 28. They turn out to be the same positions already deduced for a single spiral, *i.e.* a single sinusoid.

6.7.4. *Reduced scheme representation.* This representation can be simplified and in particular the multiple representation of the Ewald plane can be reduced to two lines, by replacing the extended scheme by a reduced one, similar to the procedure used in discussing one-dimensional Brillouin zones. This reduction is obtained by dividing the chart of Fig. 28 into vertical strips 2π wide and subsequently superposing all these strips in one basic interval, for instance $(-\pi, +\pi)$. The periodic sequences of lines representing the Ewald plane are then reduced to two lines in the interval $(-\pi, +\pi)$ and differing π in azimuth, which are the two intersections of the same plane with the projection cylinder. All α values of intersection points are now found by intersecting the reduced scheme of curves by two lines as in the lower part of Fig. 28.

It is worth noting that in most cases (*i.e.* for the most frequently occurring ϕ_0 cases) the six sinusoids of the extended scheme reduce to a single set of curved segments in the reduced scheme, at least for the commensurate cases ($2\phi_0 \simeq 10°$; $2\phi_0 \simeq 20°$). This allows one to understand why in such cases the actual diffraction pattern contains a surprisingly small number of spots.

In the reduced scheme, double points of the spherical spiral, *i.e.* points where the spiral intersects itself, actually become intersection points of curve segments. The Ewald plane, represented by the two lines (*a*) and (*b*) in Fig. 28 (bottom), passes through the double points of the curves; it is clearly a symmetry plane of the complete configuration. The spots produced in the DP are those represented in Fig. 28 to the left (top). If the Ewald plane is the one represented by the lines (*c*) and (*d*) in Fig. 28 (bottom), the produced spots are represented in Fig. 28 to the right (top). The symmetry is completely lost if the Ewald plane occupies an intermediate position, the diffraction pattern then becomes as shown for instance in Fig. 10.

So far, the Ewald plane was assumed to be parallel to the fibre axis and use was made of plots of $\sin\alpha$ *versus* ψ. For a general orientation ($\psi_{0,E}, \gamma$) of the Ewald plane, it is more convenient to plot α *versus* ψ for the diffraction loci in a reduced scheme as well as for the Ewald-plane representation. For such a plot, the sinusoid becomes a 'sawtooth' with rounded corners. Superposing the two graphs leads to Fig. 30 for the case $2\phi_0 = 19°$ and to Fig. 31 for the case $2\phi_0 = 9°$. Different inclination angles $\gamma = 0, 10, \ldots, 90°$ are represented. The α and ψ of the intersection points can now be read directly from the graphs for different inclinations of the Ewald plane. In these graphs, the azimuth of the Ewald plane $\psi_{0,E}$ was assumed to coincide with ψ_0. If this is not the case, the appropriate value of $\psi_{0,E}$ has to be used, resulting in a parallel shift of the net of Ewald planes along the ψ axis.

In particular, these graphs allow one to understand why the configuration of spots is in general complicated and asymmetric. Also, it shows how curved diffuse spots can result (as in Fig. 5), where the Ewald plane touches the spherical spirals as well as the diffuse V surface. Comparing Fig. 30 with Fig. 31 shows that the number of spots increases with decreasing ϕ_0.

7. Conical graphite fibres

In Amelinckx *et al.* (1992) and Luyten *et al.* (1993), [00.1]-zone diffraction patterns of conically wound graphite needles were discussed and analysed based on the approximation that the composite texture pattern is the superposition of the diffraction patterns of planar [00.1] sheets that are rotated with respect to the adjacent one over the angle $\beta = 2\pi - \theta$ (in the present notation). The observed azimuth spot positions φ were found to be well represented by the relation $\varphi_{k,n} = k\beta + n \times 60°$ ($n = 0, 1, 2, 3, 4, 5$), where k is an integer and β is in the range $\beta = 22$–$24°$, the cone angle ϕ_0 being in all cases close to 70°. Note that $\beta = 2\pi(1 - \sin\phi_0)$ (*), *i.e.* $\beta = 22$–$23°$. The present analysis should in particular apply to this case. The diffraction spot positions in the (0001) zone are obtained as a planar section of the diffraction space loci by a plane (the Ewald plane) perpendicular to the cone axis. For one node, the positions are thus given

by the zeros of α_n, *i.e.* by $\psi = k(\pi/\sin\phi_0)$ or, making use of (*), by

$$\psi_k = k\pi/[1 - (\beta/2\pi)] \simeq k\pi(1 + \beta/2\pi) \quad \text{since } \beta/2\pi \ll 1 \qquad (53)$$

or, finally, by

$$\psi_k = k\pi + k\beta/2. \qquad (54)$$

The spots in the sequence originating in a given $hk0$ spot are thus equally spaced by β, in accordance with the analyses in Amelinckx *et al.* (1992) and Luyten *et al.* (1993). To realise this, it is convenient to separate the ψ_k into two classes of basic spots corresponding with even (e) and odd (o) values of k:

$$\begin{aligned} k &= 2m, & \psi_e &= 2m\pi + m\beta \\ k &= 2m + 1, & \psi_o &= 2m\pi + m\beta + (\pi + \beta/2), \end{aligned} \qquad (55)$$

from which it is clear that the second sequence has the same structure as the first but is shifted in azimuth over a constant angle $\pi + \beta/2$.

The locus of a single node thus oscillates between two small circles of the sphere defined by $\alpha_{max} = +20°$ and $-20°$. The locus is a spherical spiral between these two circles. The other nodes corresponding to the same interplanar spacing describe similar loci on the same sphere. The successive loci are shifted in azimuth by 60°. The spirals intersect the Ewald plane under a rather small angle, thus leading to spots that are smeared out along the locus, as observed in Amelinckx *et al.* (1992) and Luyten *et al.* (1993).

In terms of the considerations of §6.4.7, which are applicable here, one finds for this particular case $1/\sin\phi_0 = 1.06$ and hence $N = 1$; $\varepsilon = 0.06$. The sequence of spots has a spacing $\Delta\psi = 2\pi\varepsilon$ (since N = odd). One finds $2\pi\varepsilon = 21.6°$, in agreement with the spacing deduced empirically from the observed diffraction pattern in Amelinckx *et al.* (1992).

8. Discussion and conclusions

The electron diffraction patterns produced by different microstructures of natural and synthetic chryostiles can consistently be explained by considering the loci, generated by the reciprocal-lattice nodes, as a consequence of the variation in orientation of the local lattice. In particular, the diffraction effects produced by conically wound fibres are explained in detail. It is shown that the geometry of the microstructure causes each reciprocal-lattice node to describe a spherical spiral. With a cylindrical projection method, the configuration of diffraction spots can be discussed graphically as the intersection points of the spatial configuration of spherical spirals with the Ewald plane. Excellent agreement with the experimental patterns is found. From lattice fringes and diffraction patterns, superperiods along the local c

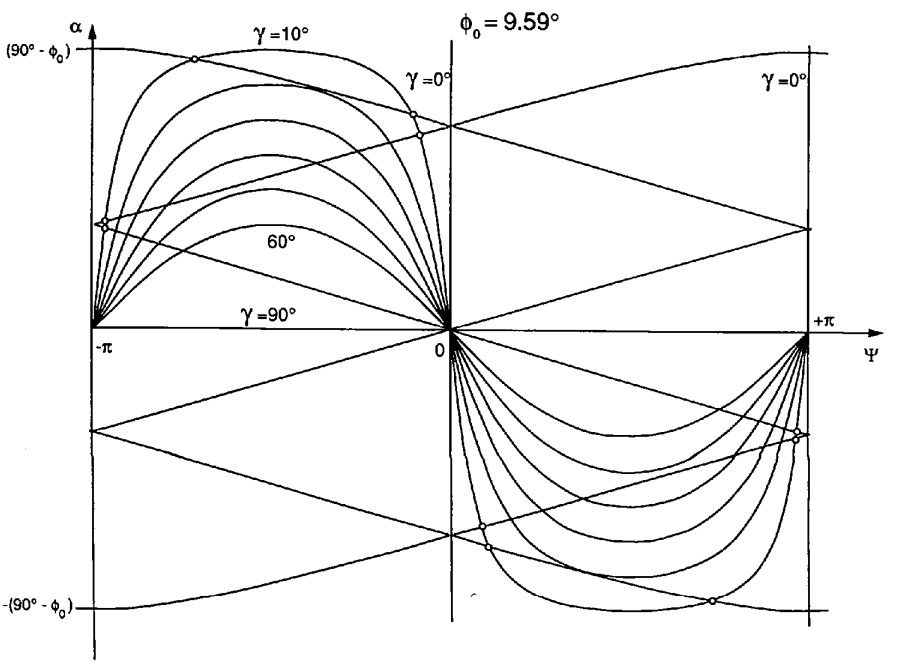

Fig. 30. Reduced scheme (α *versus* ψ) of the cylindrical projection of Fig. 29 with expanded scale along ψ ($2\phi_0 = 19°$). Superposed are the cylindrical projections of the Ewald plane in the same coordinate system for different γ values. The figure shows the special case where $\psi_{0,E} = 0$. If $\psi_{0,E} \neq 0$, the set of curves has to be shifted over $\psi_{0,E}$ along the ψ axis, with respect to the reduced scheme of the loci.

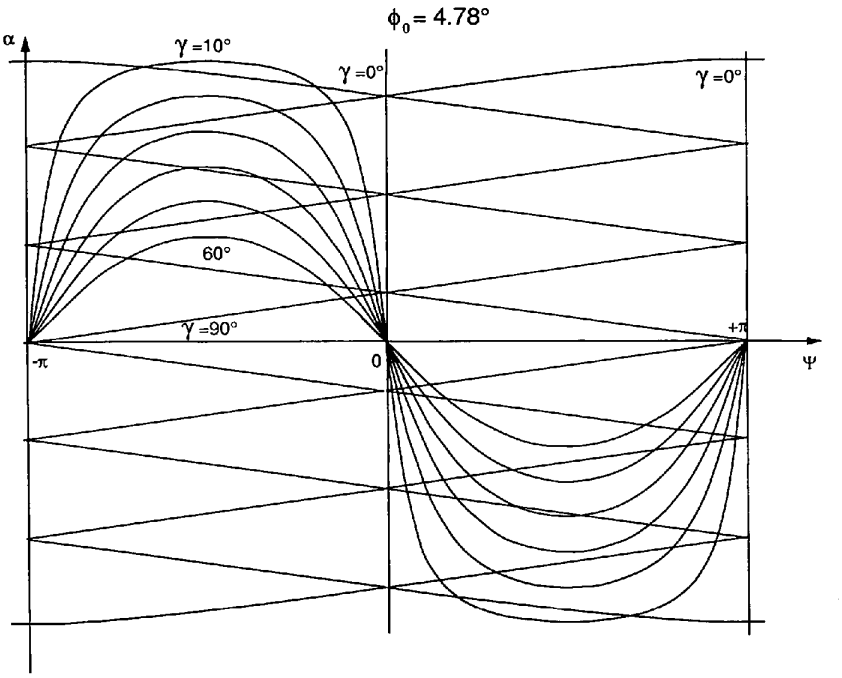

Fig. 31. Reduced scheme of the cylindrical projection (α *versus* ψ) of the six spherical spirals due to nodes of the first hexagon for a cone angle $2\phi_0 \simeq 9°$. The cylindrical projections of Ewald planes for different inclination angles are superposed on the reduced scheme of loci using the same reference system. In this graph, $\psi_{0,E} = 0$; if $\psi_{0,E} \neq 0$, the set of curves has to be shifted along the ψ axis, relative to the loci. The intersection points represent the spherical coordinates (α, ψ) of the diffraction spots.

direction are found to be consistent with the wrapping up of multilayered sheets.

In our derivation of the geometrical loci in diffraction space, we neglected the fact that the local unit cells may be different in shape (at constant volume) in successive layers of an ideal scroll. This would result from the systematic relative tangential shifts of successive layers, by a constant amount, owing to the increase in length of successive turns of the scroll ($2\pi \times$ layer thickness!). For an ideal achiral circular cylinder, this effect can readily be taken into account, as was done by Devouard (1995) and Devouard & Baronet (1996); it leads to a fine structure of the diffuse coronae mentioned in §5.2.1. This fine structure may provide an alternative interpretation for the reinforcements in streaks in the diffraction patterns in Figs. 11 and 12, assuming that they have scroll character.

A similar effect should occur in ideal conical scrolls where, apart from considered rotations between successive layers, parallel translations may also occur, in particular in high-symmetry cases. This problem remains to be solved.

In our models, we implicitly assumed random rather than systematic relative shifts; the good correspondence with the observations seems to suggest that this assumption is not unreasonable. Formulated in dislocation language, this means that the partial edge dislocations, parallel to the fibre axis, which make up the lattice curvature, are rather more randomly distributed around some average separation along the successive turns than systematically arranged, for instance in dislocation walls.

One of us (BD) wishes to thank Professor G. Van Tendeloo for giving him the opportunity to pursue these observations on serpentines in the EMAT Laboratory (Antwerp), and Dr L. Nistor for her friendly help with operating the JEOL 4000 and Philips CM-20 microscopes in the same laboratory.

References

Amelinckx, S., Bernaerts, D., Zhang, X. B., Van Tendeloo, G. & Van Landuyt, J. (1995). *Science*, **267**, 1334–1338.

Amelinckx, S., Luyten, W., Krekels, T., Van Tendeloo, G. & Van Landuyt, J. (1992). *J. Cryst. Growth*, **121**, 543–558.

Amelinckx, S., Zhang, X. B., Bernaerts, D., Zhang, X. F., Ivanov, V. & Nagy, J. B. (1994). *Science*, **265**, 635–639.

Bailey, S. W. (1969). *Clays Clay Miner.* **17**, 355–371.

Bailey, S. W. (1988*a*). *Hydrous Phyllosilicates*, edited by S. W. Bailey, Ch. 1. *Reviews in Mineralogy*, Vol. 19. Washington: Mineralogical Society of America.

Bailey, S. W. (1988*b*). *Hydrous Phyllosilicates*, edited by S. W. Bailey, Ch. 2. *Reviews in Mineralogy*, Vol. 19. Washington: Mineralogical Society of America.

Bailey, S. W. (1988*c*). *Hydrous Phyllosilicates*, edited by S. W. Bailey, Ch. 6. *Reviews in Mineralogy*, Vol. 19. Washington: Mineralogical Society of America.
Baker, R. T. K. (1989). *Carbon*, **27**, 315–324.
Baronnet, A. & Mellini, M. (1992). 29th International Geological Congress, Kyoto, Japan, Vol. 3, pp. 682–685.
Baronnet, A., Mellini, M. & Devouard, B. (1994). *Phys. Chem. Miner.* **21**, 330–343.
Chisholm, J. E. (1988). *Acta Cryst.* A**44**, 70–75.
Cressley, B. A. & Whittaker, E. J. W. (1993). *Mineral Mag.* **57**, 729–732.
Cullen, S. L., Boothroyd, C. B. & Humphreys, C. J. (1994). *Ultramicroscopy*, **56**, 127.
Devouard, B. (1995). Thesis, University of Marseille, France.
Devouard, B. (1996). In preparation.
Devouard, B. & Baronnet, A. (1996). *Eur. J. Mineral.* In the press.
Ebbesen, T. W. (1994). *Annu. Rev. Mater. Sci.* **24**, 235.
Iijima, S. (1991). *Nature (London)*, **354**, 56–58.
Iijima, S. & Ajayan, P. M. (1992). *Phys. Rev. Lett.* **69**, 3100–3104.
Iijima, S. & Ichihashi, T. (1992). *Nature (London)*, **356**, 776–779.
Jagodzinski, H. & Kunze, G. (1954*a*). *N. Jahrb. Mineral. Monatsh.* pp. 95–108.
Jagodzinski, H. & Kunze, G. (1954*b*). *N. Jahrb. Mineral. Monatsh.* pp. 137–150.
Liu, M. & Cowley, J. M. (1994*a*). *Carbon*, **32**, 393–401.
Liu, M. & Cowley, J. M. (1994*b*). *Untramicroscopy*, **53**, 333–338.
Luyten, W., Krekels, T., Amelinckx, S., Van Tendeloo, G., Van Dyck, D. & Van Landuyt, J. (1993). *Ultramicroscopy*, **49**, 123–131.
Margulis, L., Dluzewski, Y., Feldman, X. & Tenne, R. (1996). *J. Microsc.* **181**, 68–72.
Mellini, M. (1982). *Am. Mineral.* **67**, 587–598.
Mellini, M. & Zanazzi, P. F. (1987). *Am. Mineral.* **72**, 943–948.
Middleton, A. P. & Whittaker, E. J. W. (1976). *Can. Mineral.* **14**, 301–306.
Rodriguez, N. M. (1993). *J. Mater. Res.* **8**, 3233.
Tibbets, C. G. (1984). *J. Cryst. Growth*, **66**, 632.
Whittaker, E. J. W. (1952). *Acta Cryst.* **5**, 143–144.
Whittaker, E. J. W. (1953). *Acta Cryst.* **6**, 747–748.
Whittaker, E. J. W. (1954). *Acta Cryst.* **7**, 827–832.
Whittaker, E. J. W. (1955*a*). *Acta Cryst.* **8**, 261–265.
Whittaker, E. J. W. (1955*b*). *Acta Cryst.* **8**, 265–271.
Whittaker, E. J. W. (1955*c*). *Acta Cryst.* **8**, 571–574, 726–729
Whittaker, E. J. W. (1956). *Acta Cryst.* **9**, 855–861, 862–864, 865–867.
Whittaker, E. J. W. (1957). *Acta Cryst.* **10**, 149–156.
Williams, T. B. & Hyde, B. G. (1988). *Phys. Chem. Miner.* **15**, 521–544.
Yada, K. (1967). *Acta Cryst.* **23**, 704–707.
Yada, K. (1971). *Acta Cryst.* A**27**, 659–664.
Yada, K. (1979). *Can. Mineral.* **17**, 679–691.
Yada, K. & Iishi, K. (1977). *Am. Mineral.* **62**, 958–965.
Zhang, X. B., Zhang, X. F., Amelinckx, S., Van Tendeloo, G. & Van Landuyt, J. (1994). *Ultramicroscopy*, **54**, 237–249.
Zhang, X. F., Zhang, X. B., Van Tendeloo, G., Amelinckx, S., Op de Beeck, M. & Van Landuyt, J. (1993). *J. Cryst. Growth*, **130**, 368–382.
Zussmann, J., Brindley, G. W. & Comer, J. J. (1957). *Am. Mineral.* **42**, 133–153.